



Cite this: DOI: 10.1039/d0cs01060j

# On-surface synthesis of graphene nanostructures with $\pi$ -magnetism†

Shaotang Song, <sup>ab</sup> Jie Su, <sup>bc</sup> Mykola Telychko, <sup>bc</sup> Jing Li, <sup>b</sup> Guangwu Li, <sup>b</sup> Ying Li, <sup>a</sup> Chenliang Su, <sup>\*a</sup> Jishan Wu <sup>\*b</sup> and Jiong Lu <sup>\*bc</sup>

Graphene nanostructures (GNs) including graphene nanoribbons and nanoflakes have attracted tremendous interest in the field of chemistry and materials science due to their fascinating electronic, optical and magnetic properties. Among them, zigzag-edged GNs (ZGNs) with precisely-tunable  $\pi$ -magnetism hold great potential for applications in spintronics and quantum devices. To improve the stability and processability of ZGNs, substitutional groups are often introduced to protect the reactive edges in organic synthesis, which renders the study of their intrinsic properties difficult. In contrast to the conventional wet-chemistry method, on-surface bottom-up synthesis presents a promising approach for the fabrication of both unsubstituted ZGNs and functionalized ZGNs with atomic precision via surface-catalyzed transformation of rationally-designed precursors. The structural and spin-polarized electronic properties of these ZGNs can then be characterized with sub-molecular resolution by means of scanning probe microscopy techniques. This review aims to highlight recent advances in the on-surface synthesis and characterization of a diversity of ZGNs with  $\pi$ -magnetism. We also discuss the important role of precursor design and reaction stimuli in the on-surface synthesis of ZGNs and their  $\pi$ -magnetism origin. Finally, we will highlight the existing challenges and future perspective surrounding the synthesis of novel open-shell ZGNs towards next-generation quantum technology.

Received 21st October 2020

DOI: 10.1039/d0cs01060j

[rsc.li/chem-soc-rev](http://rsc.li/chem-soc-rev)

<sup>a</sup> SZU-NUS Collaborative Center, International Collaborative Laboratory of 2D Materials for Optoelectronic Science & Technology of Ministry of Education, Engineering Technology Research Center for 2D Materials Information Functional Devices and Systems of Guangdong Province, Institute of Microscale Optoelectronics, Shenzhen University, Shen Zhen, 518060, China. E-mail: [chmsuc@szu.edu.cn](mailto:chmsuc@szu.edu.cn)

<sup>b</sup> Department of Chemistry, National University of Singapore, 3 Science Drive 3, Singapore 117543, Singapore. E-mail: [chmluj@nus.edu.sg](mailto:chmluj@nus.edu.sg), [chmwuj@nus.edu.sg](mailto:chmwuj@nus.edu.sg)

<sup>c</sup> Centre for Advanced 2D Materials (CA2DM), National University of Singapore, 6 Science Drive 2, Singapore 117546, Singapore

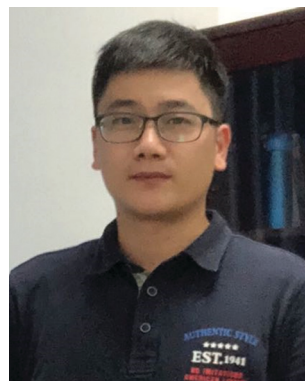
† Electronic supplementary information (ESI) available: See DOI: 10.1039/d0cs01060j



**Shaotang Song**

*nanostructures via a combination of organic synthesis and scanning tunnelling microscopy.*

*Dr Shaotang Song received his MSc in 2014 from the Beijing Institute of Technology (with prof. Li Li) and PhD in 2017 from Kyoto University (with prof. Hiroshi Sakaguchi). He joined the groups of Hiromitsu Maeda at Ritsumeikan University in 2018 and, afterwards, Jiong Lu at the National University of Singapore for postdoctoral research. His current research focuses on the bottom-up on-surface synthesis and characterization of graphene*



**Chenliang Su**

*Technology (ICL-2D MOST), Shenzhen University and a Principal Investigator of the ICL-2D MOST in materials science. His current interests include the study of nanostructured materials for heterogeneous catalysis and energy-related applications.*

*Prof. Chenliang Su received his BS degree (2005) and PhD degree (2010) from the Department of Chemistry at the Zhejiang University of China. After that he worked as a research fellow at the Advanced 2D Materials and Graphene Research Centre at the National University of Singapore (2010–2015). He is now a full-professor at the International Collaborative Laboratory of 2D Materials for Optoelectronics Science and*

# 1. Introduction

Graphene consists of a single layer of carbon atoms arranged in the honeycomb lattice, which can be viewed as a bipartite lattice composed of two interpenetrating triangular sublattices (Fig. 1).<sup>1,2</sup> As a result of lattice symmetry, the conduction and valence bands touch at the so-called Dirac point with a linear band dispersion that resembles the Dirac spectrum for massless fermions. Owing to its unusual electronic spectrum, graphene has led to the emergence of a new paradigm of quantum relativistic phenomena and novel device characteristics.<sup>3</sup> However, the lack of an energy gap has limited the applications of graphene in digital electronics. One strategy for opening bandgap is reducing the lateral dimension of graphene into nanoscale, creating graphene nanostructures (e.g., graphene nanoribbons (GNRs), graphene quantum dots (GQDs) or polycyclic aromatic hydrocarbons (PAHs)) due to quantum confinement and edge effects, which is useful for realizing the potential of graphene as a transistor.<sup>1,4–6</sup>

In addition to bandgap engineering, reducing lateral dimension of graphene *via* clipping graphene along different crystallographic orientations leads to the formation a diversity of GNs with unique electronic and magnetic properties, which depend on their sizes, shapes, and edge topologies (Fig. 1). While zigzag edges consist of carbon atoms belonging to the same sublattice, armchair edges are composed of carbon atoms from two different sublattices. These edge configurations of graphene's  $\pi$ -electron network have a significant impact on the electronic and magnetic properties of GNs. For example, armchair-edged GNRs exhibit a quantum confinement induced electronic band gap that selectively depends on the ribbon width, critical for

their applications in digital electronics. In contrast, zigzag-edged GNs (ZGNs) have been predicted to possess unpaired  $\pi$ -electrons with spin-polarized edge states. Electronic Coulomb repulsion in ZGNs can result in the formation of spin polarized electronic structures with an energy gap.<sup>7,8</sup> In addition, these ZGNs also show the geometry- and size-dependent spin transport properties. For example, triangulene homologues possess ferromagnetically coupled edge states, which can be further tuned by size engineering, in-plane electric field and chemical doping. Therefore, this class of materials has been proposed as a promising candidate for spintronics applications including spin filter, spin valve, and spin switch.<sup>9–11</sup> Moreover, graphene nanorings consisting of zigzag-edged GNR (ZGNR) was proposed to be used as active channel materials for quantum interference transistors with a high on/off ratio.<sup>9</sup>

Magnetism in ZGNs has drawn increased interest due to their potential applications in organic magnetism, MRI contrast agents, and organic spintronics.<sup>10–13</sup> In contrast to the conventional magnetic materials involving d- or f-block elements, magnetism in GNs containing light p-block carbon atoms is usually attributed to unpaired  $\pi$ -electrons or partially filled  $\pi$ -band originated from their unique topologies.<sup>14–16</sup> These ZGNs can be classified into four categories depending on the origin of  $\pi$ -magnetism. (i) Non-Kekulé ZGNs with sublattice imbalance in the bipartite honeycomb lattice. For this class of materials, no Kekulé covalence structures can be drawn without leaving unpaired electrons.<sup>17</sup> The magnetism of the non-Kekulé structure is rooted in an inherent sublattice imbalance in the bipartite honeycomb lattice, such that not all  $p_z$  electrons can be paired to form  $\pi$  bonds, thus generating uncompensated radicals.<sup>18</sup> (ii) Topological frustration induced



**Jishan Wu**

*Prof. Jishan Wu, Department of Chemistry at NUS, is a synthetic chemist and material scientist. His research interests include novel aromatic and supramolecular systems and materials. In recent years, his group developed a niche research area on open-shell singlet diradicaloids/polyradicaloids, which can be used as next generation molecular materials for electronics, photonics and spintronics. His group reported a number of open-shell graphene-like molecules which*

*provide important insight into the carbon-based magnetism. He holds total about 280 publications, which received high citation (total citations: 18 800+, H index: 68 based on Google Scholar). He has received 20 awards including the NUS Young Investigator Award (2007), Singapore Young Scientist Award (2010), NUS Young Researcher Award (2012), Dean's Chair Professorship (2014) and NRF Investigatorship (2019). He was listed as one of the highly cited researchers (cross field) from the Clarivate Analytics.*



**Jiong Lu**

*Prof. Jiong Lu holds assistant professorship at the Department of Chemistry, Centre for Advanced 2D Materials, National University of Singapore (NUS). He received his Bachelor's degree from Fudan University, PhD degree from NUS, and then did postdoctoral research in Department of Physics, University of California, Berkeley. His current research interests include atomic-scale imaging and characterization of 2D materials and their devices, and on-surface synthesis of open-shell graphene nanostructures.*

unconventional magnetism in GNs which can be explained by the concept of “nullity” ( $\eta$ ) defined by their topologies. “Nullity” ( $\eta$ ), is determined by the topology of GN through the equation:  $\eta = \alpha - \beta$ , where  $\alpha$  and  $\beta$  are the maximum number of nonadjacent vertices and edges, respectively.<sup>18</sup> The inability to simultaneously pair all  $p_z$  orbitals is attributed to the topological frustration of GNs, which can be classified into two sets: involving only one or both two sublattices. Clar’s goblet with two topologically frustrated sublattices is thus classified as the second one (discussed in Section 4.7). (iii) ZGNs with resonance structures of both Kekulé and non-Kekulé forms. This class of materials also don’t possess sublattice imbalance. According to Clar’s rule, the resonance structure of a GN with the maximum number of Clar sextet (defined as six  $\pi$ -electrons localized in a single hexagonal ring separated from adjacent rings by C–C single bonds, as represented by the color filled hexagonal rings in Fig. 1 and Fig. 15) is considered as the most stable form by gaining the extra aromatic stabilization energy.<sup>19,20</sup> The magnetism (radical character in non-Kekulé format) is driven by the maximization of the number of Clar’s sextet (the most stable form), which is a result of gaining aromatic stabilization energies. Zethrenes, a representative example, show a closed-shell quinoidal form and open-shell diradical form, and its diradical character is closely related to the number of Clar’s sextet (Fig. 1). (iv) ZGNs are predicted to host low-energy spin-localized states, which shift towards Fermi level as their size increases.<sup>7,8</sup> Coulomb repulsion triggers the spin polarization for the induced magnetism in ZGNs. Such a

trend has been experimentally demonstrated in a recent work (discussed in Section 4.8 of this review) that reports a closed-shell [4]rhombene and an open-shell [5]rhombene.

Although spin-polarized edge states in ZGNs (*e.g.*, triangulenes and ZGNRs) have long been predicted,<sup>15,21</sup> a direct verification of their magnetic properties has remained elusive.<sup>16</sup> The chemical synthesis of ZGNs also presents a grand challenge due to their high chemical reactivity arising from the presence of unpaired electrons. Up to date, only substituted ZGNs were synthesized *via* conventional solution-phase chemistry.<sup>22,23</sup> In addition, ZGNs can also be fabricated *via* the “top-down” method involving clipping graphene into nanometer-sized structures by means of lithography or plasma treatment. However, these ZGNs synthesized *via* these top-down methods generally lack atomic precision.<sup>21,24</sup>

On the other hand, on-surface bottom-up synthesis relying on the rational design of molecular precursors and subsequent surface-assisted methods to produce GNs with desired topologies, is gaining intensive research interest in this field. The on-surface synthesis can be steered by a variety of factors including rational precursor design, a choice of catalytic substrates and external reaction triggers. The latter includes thermal annealing protocols, light irradiation and tip manipulation in a scanning tunneling microscope (STM). Such a bottom-up approach offers a viable route towards the synthesis of atomically precise ZGNs. Recent advances in tip-functionalized STM and non-contact atomic force microscopy (nc-AFM) imaging allow for the characterization of the structural and electronic properties of these GNs with unprecedented sub-molecular resolution.<sup>25,26</sup>

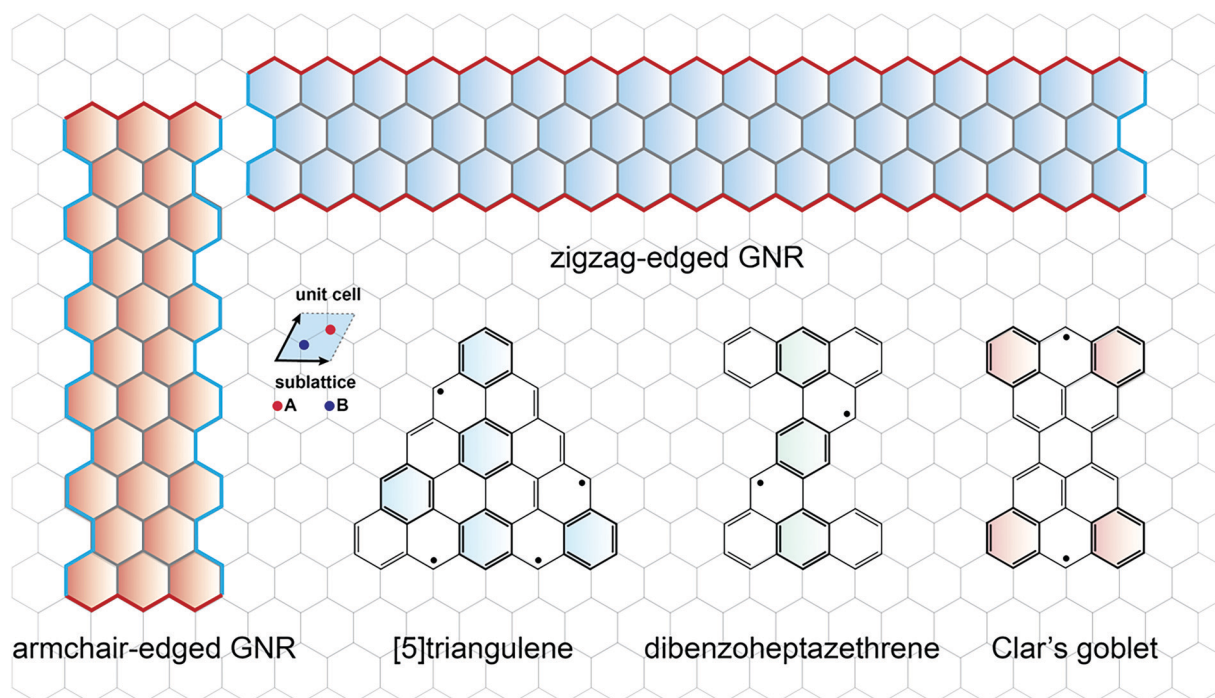


**Fig. 1** Schematic illustration of various zigzag-edged graphene nanostructures. The zigzag and armchair edges are highlighted by red and blue lines, respectively. The orange and blue filled circles represent two sublattices in a graphene unit cell. Clar sextets are highlighted with color filled hexagonal rings in the [5]triangulene, dibenzoheptazethrene, and Clar's goblet.



The synthesis and characterization of open-shell GNs with zigzag edges have evolved into one of the most active research topics. Although several reviews have been published on the topic related to the synthesis of GNs, most of them focus on the closed-shell GNs or on the synthetic design of the zigzag topologies of GNs.<sup>27,28</sup> Moreover, magnetism in two-dimensional materials,<sup>29</sup> solution-synthesized molecules,<sup>30</sup> and their theoretical models<sup>14</sup> have been reviewed. However, the on-surface synthesis of open-shell GNs, together with the detailed mechanism of their magnetism origin, the open-shell electronic structure engineering, and their potential applications have not been systematically highlighted. In this review, we will discuss these topics and highlight the recent advances in on-surface synthesis of various open-shell GNs under the four categories as described above: (i) sublattice imbalance, including: (1) triangulene, (2) extended triangulene, (3) triangulene quantum ring, (4) triangulene dimer. (ii) topological frustration, including: (5) Clar's goblet. (iii) aromatic stabilization, including: (6) super-heptazetherene, (iv) size-dependent magnetism, including (7) higher order acenes, (8)  $[n]$ rhombene, (9)  $[n]$ coronene. In addition, (10) *peri*-acene, (11) short zigzag termini of AGNRs, (12) zigzag-edged GNRs, (13) GNR junctions, (14) porphyrin derivatives are also included.

## 2. Potential applications of open-shell GNs

Spintronics exploits the spin degree of freedom to inject, transport, and detect information in devices, differs from traditional electronics that utilizes the charge-based carriers.<sup>31,32</sup> Specifically, open-shell GNs possess outstanding  $\pi$ -magnetism which makes them promising candidates for spintronics applications. Firstly, the magnetic properties of GNs can be precisely engineered by a judicious design of their topologies. Secondly, GNs exhibit a long spin-lifetime and spin-diffusion length, due to their weak spin-orbit coupling and hyperfine interaction.<sup>33–36</sup> Thirdly, GNs can be potentially “welded” with graphene-based contacts, thus circumventing an undesirable spin-depolarization at contact-semiconductor interface in the solid-state spintronic device.<sup>37,38</sup> A few conceptual implementations of GNs into such a spintronic devices, including spin filters, and logical gate are depicted schematically in Fig. 2. Several GNs with designed geometries have been proposed for spin logic operations.<sup>18,39</sup> For instance, the bow-tie- and rhombus-shaped GNs (described in Sections 4.7 and 4.8) adopt anti-ferromagnetic singlet ground state spin configuration. Therefore, these GNs can be potentially employed for the realization of a NOT logic gate unit, since flipping the input spins on one termini of the molecule requires the output spins on the other termini to flip as well.<sup>18</sup> Furthermore, the coupling strength between the two termini can be further engineered by a rational design of their topologies.

Apart from the spin-logic gate, various GNs with different topologies have been proposed as key components for the spin filter device.<sup>37,40–43</sup> For example, zigzag-edged hexagonal GNs

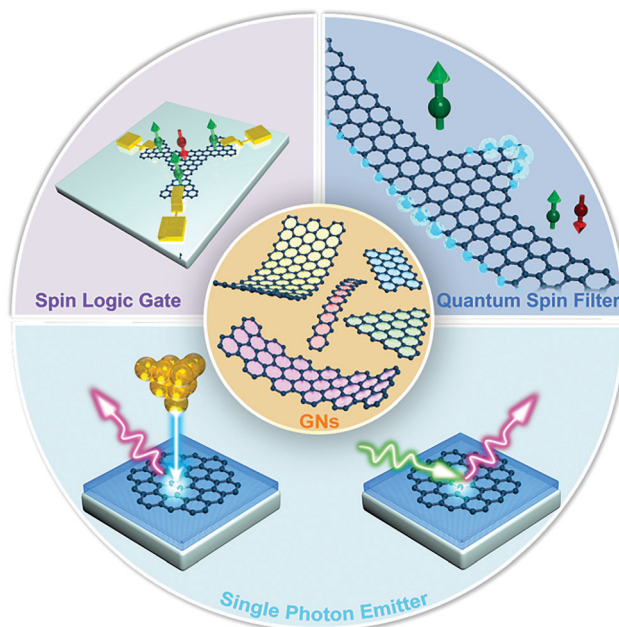


Fig. 2 Potential applications of magnetic GNs including: (i) spin logic gate; (ii) quantum spin filter; (iii) single photon emitter.

as function of different size has been theoretically studied and proposed for spin filters.<sup>44</sup> Hexagonal-shaped GNs with six identical zigzag edges favor the anti-ferromagnetically coupled edge states, which enable the spin-dependent quantum interference effects that leads to the realization of the spin-filtering operation in the absence of an external magnetic field. Recently, a high-yield synthesis of such a hexagonal-shaped molecule, namely circumcoronene, has been realized by our group (described in Section 4.9), which shed new light on the real application of hexagonal-shaped GNs in the future.

Open-shell GNs also hold a great prospect for a range of applications in quantum nanotechnology and quantum optoelectronics, wherein GNs could be used as qubits for quantum information processing,<sup>45</sup> single-photon emission sources,<sup>46,47</sup> and laser sources.<sup>48</sup> Recent experimental breakthroughs demonstrate that bottom-up fabricated GNs can act as highly efficient and stable single-photon emitters at room temperature. The emission wavelength can be tuned *via* a judicious modification of the functional groups on the GN edges.<sup>46</sup> Furthermore, it has been demonstrated that edge configuration of GNs also largely determines its photoemission quantum yield characteristics. Specifically, armchair edged GN typically show a rather low quantum yield due to symmetry-forbidden electronic transitions.<sup>48–50</sup> In contrast, zigzag-edged GNs allow for a remarkable increase of quantum yield value. In addition, according to theoretical predictions, the inherent high-spin electronic structures of some open-shell GN, such as triangulene homologues (described in Section 4.5), are expected to allow for enhanced intersystem crossing dynamics between different multiplet states, which may enhance the brightness of the triangulene-based emitters.



### 3. Principle of on-surface synthesis and precursor design

The concept of surface-assisted cross-coupling of rationally-designed organic precursors into one-dimensional (1D) chains or two-dimensional (2D) networks was demonstrated in the seminal works of L. Grill and R. Fasel respectively.<sup>51,52</sup> The substrates used for on-surface synthesis generally involve a clean single-crystal metallic surface. These metal surfaces (such as Au, Ag, Cu, Ni, Pt) act as both the template and catalytic support to facilitate the adsorption, re-organization and chemical transformation of molecular precursors into the desired products.<sup>53</sup> The strategy lies in the rational design of elegant precursors ready for the subsequent surface-assisted transformation *via* different types of chemical reactions including aryl-aryl coupling, Ullmann coupling, Glaser coupling, Sonogashira coupling, radical polymerization and oxidative cyclodehydrogenation.<sup>52,54</sup> These reactions are typically triggered by thermally-activated bond cleavage of the precursor molecules on catalytically-active substrates, which includes the breakage of carbon-halogen or carbon-hydrogen bond followed by radical polymerization and inter- or intra-molecular dehydrogenation (Fig. 3). Such an approach has been widely

used for the synthesis of GNRs and nanographene flakes<sup>55,56</sup> with both armchair and zigzag edge configurations.

Apart from thermally-activated reactions, other viable triggers include STM tip manipulation and visible-light-irradiation (Fig. 3). STM tip manipulation relies on the precise positioning of atomically-sharp tip over the specific molecular site followed by a voltage pulse to initiate chemical reactions. The underlying mechanism typically involves inelastic energy transfer from the hot electron to the target chemical bond, leading to multiple excitations.<sup>57</sup> Furthermore, the electron population of the empty state with anti-bonding character can also promote the activation of the chemical bonds.<sup>58</sup> This method has been widely used in the dissociation of oxygen, hydrogen and halogen atoms on different substrates.<sup>26,59,60</sup> Alternatively, light-irradiation produces photoexcited charge-transfer channels that promote on-surface chemical reactions such as light-induced sulphur-sulphur bond dissociation<sup>61</sup> and photopolymerization of tetraphenylporphyrin.<sup>62–64</sup> Typically, two excitation mechanisms including indirect (substrate-mediated) and direct (intra-adsorbate) one, have been proposed for the photo-induced surface reactions on metal surfaces. In the former case, hot electrons generated in the bulk metal by photoabsorption transiently enter the unoccupied states of the molecule

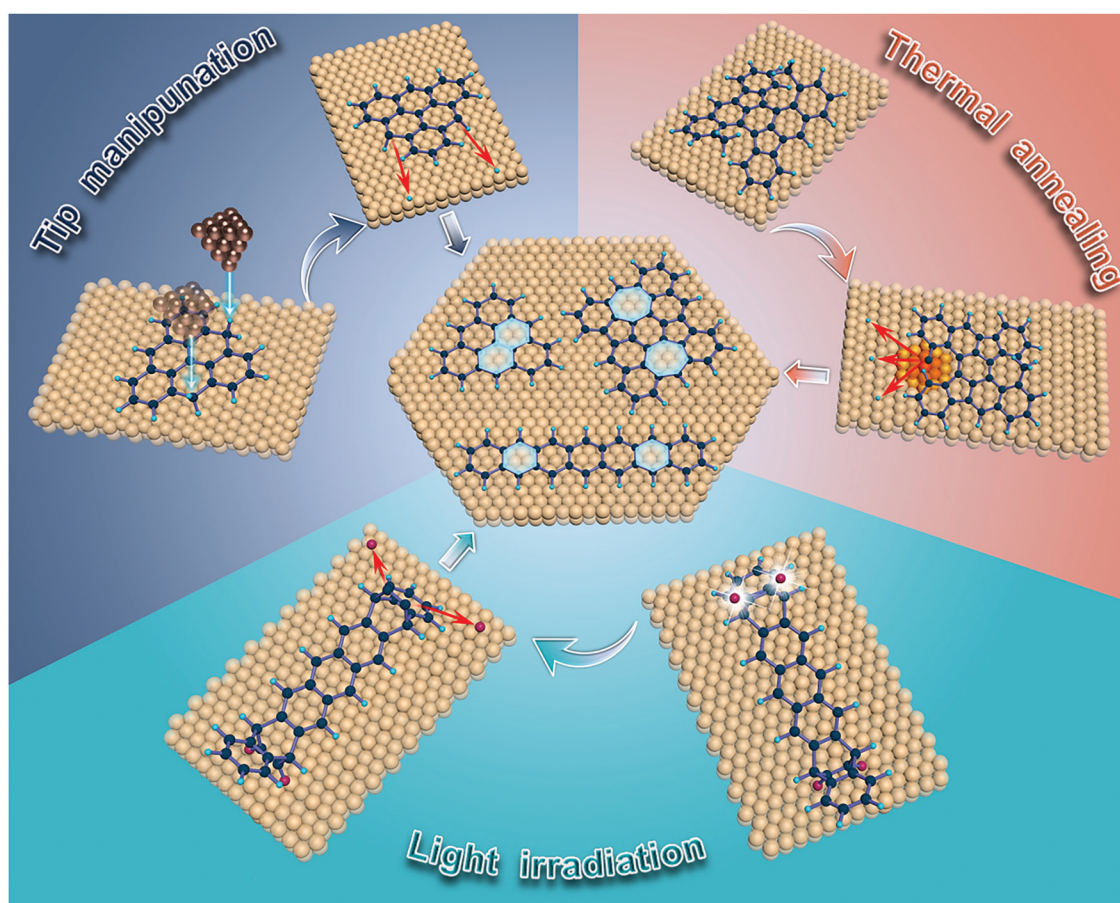


**Fig. 3** Schematic illustration of three representative on-surface synthesis protocols: thermal-annealing-induced intramolecular dehydrogenation reaction, tip-manipulation-induced deoxygenation reaction, and visible-light-irradiation induced photodecarbonylation reaction for the synthesis of azulene embedded *peri*-tetracene isomer, heptacene, and triangulene, respectively.

through an inelastic scattering process, leading to the formation of ionic species that initiate photochemical reactions.<sup>65,66</sup> In contrast, the direct mechanism relies on the photoinduced excitation of electron in the hybridized molecular frontier orbitals across the HOMO–LUMO gap of the adsorbed molecule.

The aforementioned on-surface reactions have been utilized to synthesize a majority of GNs with different types of edge configurations. In contrast to the synthesis of GNs with armchair edges, the synthesis of GNs with zigzag edges requires the design of new type of precursors because the polymerization of the monomers *via* aryl–aryl coupling predominately takes place along the zigzag rather than the armchair direction.<sup>55,56</sup> GNs with zigzag edges are typically fabricated by three different chemical routes *via* on-surface synthesis: (i) the zigzag edges are contained in the molecular precursor, such as the fabrication of *peri*-acene *via* a linear fusion of two acenes and the short zigzag termini of the AGNRs; (ii) the missing zigzag cusps in a partially formed zigzag edge can be completed by an oxidative ring closure of methyl groups with its neighboring benzene ring on the cove regions (as illustrated in Fig. 5A, 7A, and 9B); (iii) the cleavage of protecting groups or the dehydrogenation of methyl groups to generate pure zigzag edges, which has been adopted to synthesize high order acenes,<sup>68–73</sup> triangulene,<sup>74</sup> and olympicene.<sup>75</sup>

## 4. On-surface synthesis and characterization of ZGNs

### 4.1 Linear acenes

Acenes contain a series of fused benzene rings in a linear array. Despite being a  $\pi$ -extended system, one can draw only one Clar's sextet for each Kekulé resonance structure. The aromaticity shared by a greater number of rings is reduced as the acene increases in length. Because of this, longer acenes also suffer from high chemical instability. While it is generally accepted that short acenes have a closed-shell electronic ground state, electronic properties of longer acenes (longer than pentacene or hexacene) are still being debated. Earlier theoretical studies have predicted an open-shell singlet,<sup>76</sup> triplet,<sup>77</sup> and even higher spin ground states<sup>78</sup> for acenes longer than hexacene. Recent theoretical studies based on the particle–particle random-phase approximation reveal that the singlet–triplet energy gap of the acene series decreases as their length increases but the ground state of longer acenes remains as singlet.<sup>22,79–82</sup>

Apart from higher chemical reactivity, longer acenes also exhibit lower solubility, posing a challenge in solution-phase chemical synthesis. To resolve these issues, a common approach towards the wet chemical synthesis of higher order acenes involves the introduction of substituents, such as triisopropylsilylethynyl groups *etc.*, for the propose of kinetic protection and increasing solubility.<sup>22,83–88</sup> To date, several acene derivatives up to nonacene have been successfully synthesized using solution-phase chemistry.<sup>89–91</sup> UV-Vis absorption spectrum was used to monitor the lifetime of

heptacene under ambient condition, which suggests an open-shell ground state. However, it is challenging to synthesize even larger acenes.

On the other hand, on-surface synthesis of acenes, which can produce unsubstituted acenes under UHV conditions. Although shorter unsubstituted acenes ranging from tetracene to dodecacene have been successfully synthesized on surface from specifically designed precursors (Fig. 3), the design and synthesis of extended acenes with the fusion of more benzene rings still remains a grand challenge.<sup>92</sup>

The on-surface synthesis of pentacene on Ni(111) through a stepwise reaction pathway constitutes a pioneer work in this field.<sup>71</sup> STM imaging reveals a successful conversion of tetrathienoanthracene precursors (2 in Fig. 4) into pentacene *via* thermally induced sulfur abstraction and cyclization reaction. A temperature-dependent STM study suggests the following reaction steps are involved: as-deposited precursor undergoes: (i) dehalogenation (ii) ring-opening and (iii) desulfurization. Subsequently, the undercoordinated carbon atoms at each end of the desulfurized intermediate bond to one another for ring closure. This strategy can be applied to the synthesis of pentacene from a non-halogenated analogue of the tetrathienoanthracene precursor.

Krüger *et al.* reported a general method to obtain larger acenes by on-surface reduction of epoxyacenes. This method was first realized with the synthesis of tetracene from diepoxytetracene (1 in Fig. 4).<sup>68</sup> The epoxyacenes were synthesized following multistep iterative sequence of aryne cycloadditions that start from commercially available naphthodiyne or bistriflate with furan. The resulting precursor with two, three or four epoxy groups (1, 3, 9, and 12 in Fig. 4) can form tetracene, hexacene, decacene, and dodecacene, respectively upon the deoxygenation by means of either thermal annealing or STM tip manipulation.<sup>59,67–69</sup>

Hydroacenes, partially saturated acenes were also used as precursors for even higher-order acenes (5, 6, 8, 10, and 11 in Fig. 4).<sup>73,93</sup> Zuzak *et al.* developed a general method for the synthesis of hydroacenes based on the gold(I)-catalyzed cyclization of dienyne, which were assembled through a double Sonogashira cross-coupling between 1,4-diiodobenzene and terminal alkynes. The precursors of hepta-, octa-, non-, dec- and undecacene can be obtained through the cyclization reaction depending on the backbone length of the dienyne.

The corresponding acenes could then be generated either by thermal annealing of the sample or by STM tip manipulation. The latter process could be performed by applying the bias voltage with the tip apex located over the non-aromatic ring consisting of two methylene groups. The target acenes are formed *via* the dehydrogenation followed by the aromatization and planarization of the molecular fragment. The electronic gap of acenes as a function of the number of the fused benzene rings has been determined *via* the scanning tunneling spectroscopy (STS) measurements (Table 1).<sup>94</sup>

Recently, Urgel *et al.* reported a new approach towards on-surface formation of heptacene and nonacene *via* the photodecarbonylation of  $\alpha$ -bisdiketone precursors on Au(111) surface under UHV conditions. Two  $\alpha$ -bisdiketone moieties attached to

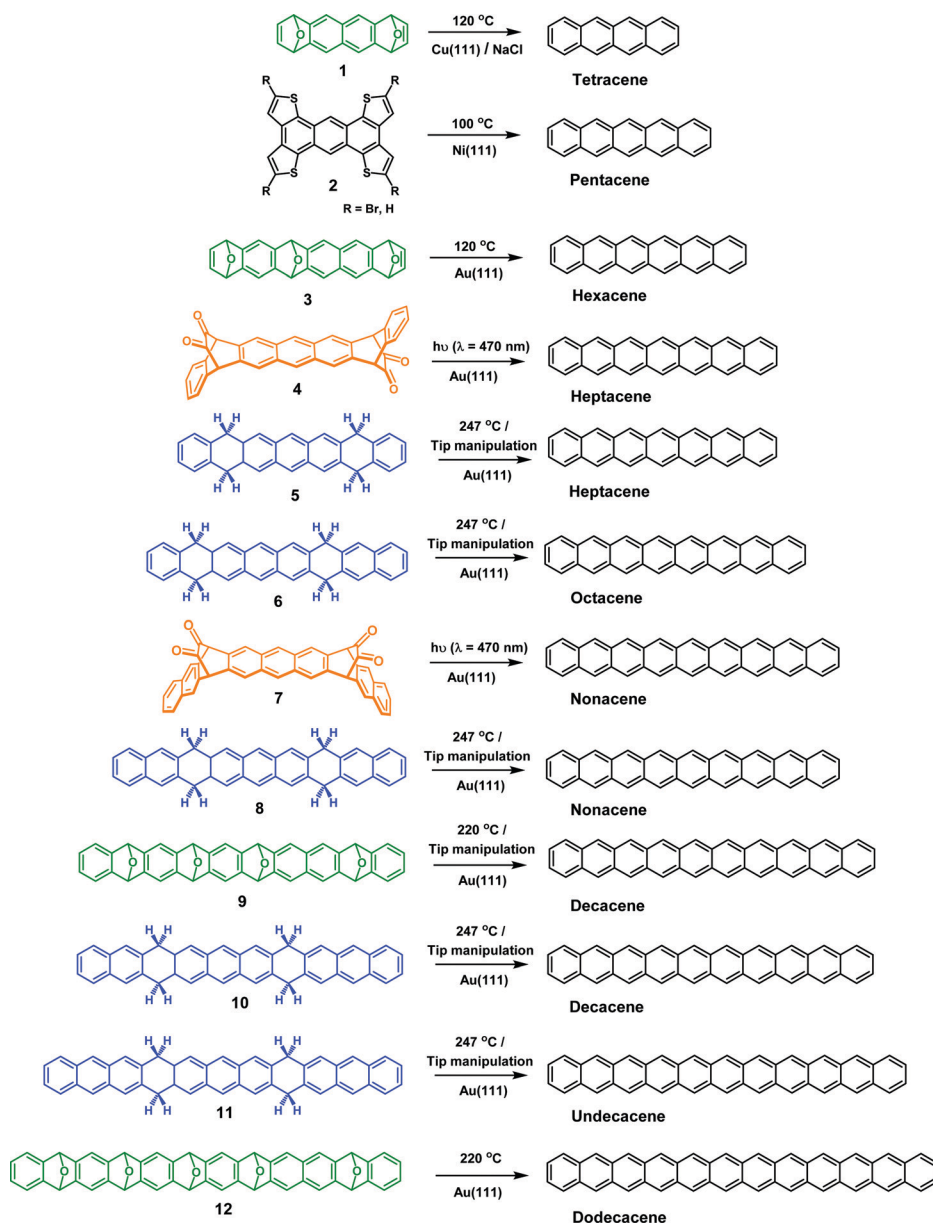


Fig. 4 On-surface synthesis of various acenes with different lengths via thermal annealing, light irradiation and STM tip manipulation.

the precursor backbone serve as protecting groups to ensure a high molecular stability and solubility. Upon irradiation with visible light (wavelength ( $\lambda_1$ ) = 470 nm), the photodecarbonylation of the precursor occurs, leading to the formation of the corresponding acenes. In addition, the cleavage of the  $\alpha$ -bisdiketone groups can also be achieved *via* STM tip manipulation.<sup>70</sup>

Urgel *et al.* have demonstrated a thermally catalytic decarbonylation of a two-Br substituted precursor for the synthesis of heptacene on Au(111).<sup>95</sup> The first-step debromination of molecular precursors leads to the formation of Au-directed organometallic polymers. Subsequently, a second annealing step activates the bisdecarbonylation of the bridging  $\alpha$ -diketone moieties, giving rise to heptacene organometallic complexes.

The synthesis of larger acenes has also been realized by designing a new precursor, 2,3-dibromotetracene.<sup>96</sup> The precursor molecules were thermally activated at the *ortho* positions to form an aryne. The subsequent cycloaddition leads to the formation of tetracene dimers with newly-formed four-member ring, cyclo-trimers and X-shaped tetramers depending on the number of arynes involved in the reaction.

Based on the above mentioned on-surface synthesis of higher acenes and their electronic structure characterization by dI/dV spectrum. It was also found that the longer acenes show smaller electronic gaps and higher chemical reactivity arising from (i) the presence of one stabilizing  $\pi$ -sextet, and (ii) reduced aromaticity *via* sextet migration as the number of benzene rings increases.<sup>97</sup>



**Table 1** A summary of the structure, electronic and magnetic properties of ZGNs synthesized on different surfaces

Name	Benzene ring number	CS/OS <sup>a</sup>	Magnetism	Band gap (eV)	Substrate
Tetracene <sup>68</sup>	4	CS	non <sup>b</sup>	—	Au(111)
Pentacene <sup>71</sup>	5	CS	non	2.20	Ni(111)
Hexacene <sup>69</sup>	6	CS	non	1.85	Au(111)
Heptacene <sup>70,95</sup>	7	CS	non	1.60	Au(111)
Octacene <sup>73</sup>	8	CS	non	1.41	Au(111)
Nonacene <sup>70,93</sup>	9	CS	non	1.23	Au(111)
Decacene <sup>59</sup>	10	CS	non	1.02	Au(111)
Undecacene <sup>94</sup>	11	CS	non	1.09	Au(111)
Dodecacene <sup>67</sup>	12	CS	non	1.40	Au(111)
<i>Peri</i> -tetracene <sup>102</sup>	11	OS	AFM <sup>c</sup>	0.35	Au(111)
<i>Peri</i> -pentacene <sup>103</sup>	14	OS	AFM	—	Au(111)
BO-doped <i>peri</i> -hexacene <sup>101</sup>	13	CS	non	—	Au(111)
Olympicene <sup>75</sup>	5	OS	PM <sup>d</sup>	—	Cu(111)
[3]Triangulene <sup>51</sup>	6	OS	FM <sup>e</sup>	3.25	Xe(111), Cu(111), NaCl
[4]Triangulene <sup>96</sup>	10	OS	FM	1.55	Au(111)
[5]Triangulene <sup>103</sup>	15	OS	FM	1.70	Au(111), Cu(111)
[7]TQR <sup>126</sup>	21	OS	FM	1.21	Au(111)
Circumcoronene <sup>136</sup>	19	CS	non	2.50	Cu(111)
6ZGNR <sup>15</sup>	—	OS	AFM	1.40	Au(111)
5-AGNR <sup>121</sup>	—	OS	PM	—	Au(111)
(7,12)-AGNR <sup>119</sup>	28	CS	non	1.90	NaCl
(7,16)-AGNR <sup>119</sup>	38	CS	non	1.90	NaCl
(7,20)-AGNR <sup>119</sup>	48	CS	non	1.90	NaCl
(7,48)-AGNR <sup>119</sup>	118	CS	non	1.90	NaCl
zeeGNR1 <sup>114</sup>	—	CS	non	1.40	Au(111)
zeeGNR2 <sup>114</sup>	—	CS	non	—	Au(111)
ETRI <sup>130</sup>	11	OS	FM	—	Au(111)
ETRI dimer <sup>130</sup>	24	OS	PM	—	Au(111)
DTRI <sup>130</sup>	14	CS	non	0.90	Au(111)
LDETRI <sup>131</sup>	24	OS	AFM	0.11	Au(111)
LDETRI with pentagon ring <sup>131</sup>	23	OS	PM	—	Au(111)
Clar's goblet <sup>113</sup>	11	OS	AFM	1.30	Au(111)
Clar's goblet dimer <sup>113</sup>	24	OS	PM	—	Au(111)
Triangulene dimer <sup>126</sup>	12	OS	AFM	1.65	Au(111)
Triangulene dimer with spacer <sup>126</sup>	13	OS	AFM	1.65	Au(111)
[4]Rhombene <sup>135</sup>	16	OS	non	0.73	Au(111)
[5]Rhombene <sup>135</sup>	25	OS	AFM	0.90	Au(111)/Ag(111)/Cu(100)
Super-heptazethrene <sup>139</sup>	12	CS	AFM	0.23	Au(111)
Zn(II)PorA <sub>4</sub> <sup>143</sup>	12	OS	PM	1.70	Au(111)
Zn(II)PorA <sub>2</sub> <sup>143</sup>	6	OS	FM	1.00	Au(111)
PorA <sub>4</sub> <sup>145</sup>	12	OS	PM	2.30	Au(111)

<sup>a</sup> CS: closed-shell; OS: open-shell. <sup>b</sup> Non: nonmagnetic. <sup>c</sup> AFM: antiferromagnetic. <sup>d</sup> PM: paramagnetic. <sup>e</sup> FM: ferromagnetic.

Despite recent success in the on-surface synthesis of higher order acenes, a direct evidence of the magnetic response for the acenes synthesized on surfaces is still missing. This is probably due to the electronic interactions of the molecule with the substrate that disfavor a direct observation of their magnetic response. It has been reported that the magnetism of a boron-doped GNR can be quenched due to the presence of metallic substrates.<sup>98</sup> In order to probe the intrinsic electronic structures of higher acenes, it is required to develop new approaches for a direct synthesis of these structures on insulating substrate or to transfer them from metallic substrate onto insulating substrates by tip manipulation.

## 4.2 *Peri*-Acenes

*Peri*-Acenes can be viewed as the lateral fusion of two linear acenes at the *peri*-position into rectangular nanographene flakes such as bisanthene, *peri*-tetracene, and *peri*-pentacene. An open-shell diradical structure accompanied by two additional aromatic sextet rings can be drawn for this series of

molecules. Theoretical calculations predict a reduction of energy gap as an increase of their length along the zigzag-edge direction.<sup>80,99</sup>

Ni *et al.* reported the successful synthesis and isolation of a stable *peri*-tetracene derivative in solution with four bulk electron-withdrawing 2,6-dichlorophenyl groups attached to the reactive zigzag edge sites.<sup>100</sup> This compound displays an open-shell singlet ground state with a moderate diradical character ( $y_0 = 51.5\%$ ). On the other hand, larger *peri*-acenes usually exhibit a greater degree of diradical character as revealed by theoretical calculations. Hence, it remains a great challenge to synthesize and isolate large-sized unsubstituted *peri*-acenes.

Recently, several groups performed on-surface synthesis of *peri*-acenes derived from rationally-designed precursors.<sup>101–103</sup> Rogers *et al.* reported the first case on the synthesis of *peri*-pentacene converted from 6,6'-bipentacene as the precursor as depicted in Fig. 5D.<sup>103</sup> The precursor bipentacene was synthesized through a Staudinger-type diazo-thioketone coupling

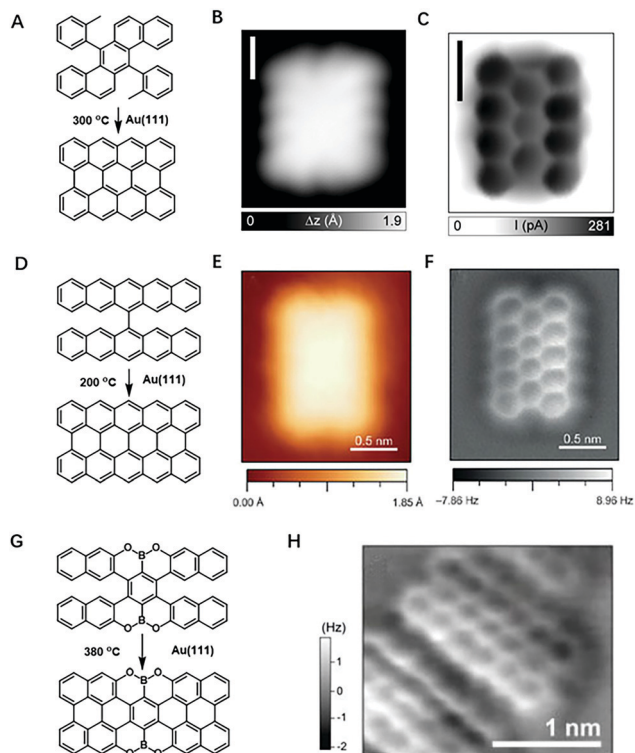


**Fig. 5** On-surface synthesis and characterization of different *peri*-acenes. (A, D, G) Illustration of the synthetic routes toward on-surface synthesis of *peri*-tetracene, *peri*-pentacene, and BO doped *peri*-hexacene, respectively. (B and C) STM and BRSTM images of *peri*-tetracene, respectively. (E and F) STM and nc-AFM images of *peri*-pentacene, respectively. (H) nc-AFM images of BO-doped *peri*-hexacene. Reproduced with permission from ref. 101–103. Copyright 2019 American Chemical Society, 2018 John Wiley and Sons.

reaction, whereby two pentacene molecules can be coupled through the central benzene rings. Thermal annealing of the deposited precursors on Au(111) at 200 °C for 30 min induces a thermal cyclodehydrogenation of all the *peri*-positions to form the fully cyclized *peri*-pentacene, as evidenced by STM and nc-AFM imaging (Fig. 5E and F).

Wang *et al.* reported the first oxygen and boron doped *peri*-hexacene with OBO (Oxygen–Boron–Oxygen bonds connected) segments on the zigzag edges *via* the surface-assisted cyclodehydrogenation of the precursor containing a double helicene connected head-to-head with two OBO segments on the edges.<sup>101</sup> The cyclodehydrogenation was initially attempted in solution with the assistance from an oxidant such as FeCl<sub>3</sub> or 2,3-dichloro-5,6-dicyano-1,4-benzoquinone. Unfortunately, a mixture of undefined products was obtained in the solution-phase. In contrast, the cyclodehydrogenation of the precursor to form OBO-doped *peri*-hexacene (Fig. 5G) was successfully achieved on Au(111) at 380 °C. It was also observed that planar *peri*-hexacene derivatives form self-assembled structures due to intermolecular hydrogen bonding [O...H] as shown in Fig. 5H. Apart from the lateral fusion of two linear acenes into *peri*-acenes, another strategy for the synthesis of *peri*-acenes involves the oxidative ring closure of molecular precursors with

methyl groups, similar to the aforementioned synthesis of ZGNR.<sup>102</sup> Using this strategy, *peri*-tetracene has been synthesized on Au(111) as depicted in Fig. 5A–C. The electronic gap of *peri*-tetracene on Au(111) was determined to be 0.35 eV *via* STS, much smaller than that of the largest dodecacene (1.4 eV) synthesized on Au(111). The *dI/dV* maps obtained with a CO-functionalized tip at the energetic positions of the highest occupied molecular orbital (HOMO) and the lowest occupied molecular orbital (LUMO) reveal localized electronic states at the zigzag edges.

### 4.3 Zigzag-edged GNRs

ZGNRs can be viewed as the lateral extension of acenes with varied width and extended length. Prior to the synthesis of ZGNRs, numerous efforts have been made on the on-surface synthesis of armchair-edged (AGNRs), heteroatoms-doped, as well as GNRs with heterojunctions.<sup>52,104–106</sup> However, the synthesis of ZGNRs demands a different precursor design strategy. This is because the polymerization of monomers *via* aryl–aryl coupling takes place along the zigzag direction<sup>107,108</sup> rather than armchair direction. Ruffieux *et al.* reported the seminal synthesis of 6-ZGNR using a specifically-designed U-shape precursor (Fig. 6A).<sup>15</sup> The precursor was functionalized with two halogen groups for the thermally-induced aryl–aryl coupling, and two methyl groups for creating two new six-membered rings *via* oxidative ring closure reaction with its neighboring benzene ring to generate continuous zigzag edges. The chemical structure of 6-ZGNRs has been clearly resolved by nc-AFM imaging (Fig. 6B). To decouple the electronic interactions between the ZGNR and the metallic surface, as-synthesized GNRs were transferred from Au(111) onto the atomically-thin insulating NaCl films deposited on Au(111) *via* atomic manipulation. The *dI/dV* spectrum taken at the edge of the decoupled ZGNR segment exhibits three resonance peaks below and above  $E_F$ , with energy splitting gaps of  $\Delta^0 = 1.5$  eV and  $\Delta^1 = 1.9$  eV between the two occupied states and the unoccupied one (Fig. 6E), in good agreement with the calculated density of states (DOS) (Fig. 6D). *dI/dV* maps acquired at these peaks reveal that the corresponding states are highly localized at the zigzag edges (Fig. 6F). The characteristic features, such as a protrusion at each outermost zigzag carbon atom and an enhanced intensity at the ribbon terminus, are in excellent agreement with the local density of states (LDOS) plots of the corresponding Kohn–Sham density functional theory (DFT) orbitals (Fig. 6G).

Although successful fabrication and characterization of the ZGNR was achieved, a direct characterization of the magnetism of the ZGNR is still missing. The spin density of ZGNR on one edge is usually balanced by a spin density of the same amplitude on the other edge resulting in zero net spin. The magnetic coupling between two opposite edges also depends on the width of ZGNR, which deserves future exploration. Collaborative effort between synthetic chemists and surface scientists is needed to design smart precursors for the on-surface synthesis of narrower ZGNRs such as 2-, 3-, 4-, and 5-ZGNR. On the other hand, the fabrication of wider ZGNRs requires the design of

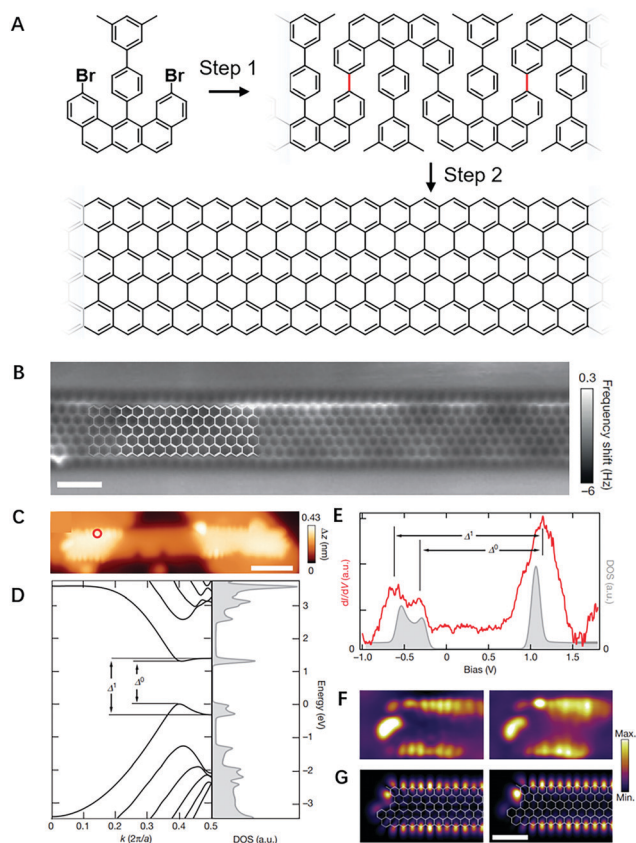


**Fig. 6** On-surface synthesis and characterization of ZGNRs. (A) Schematic illustration of the synthetic strategy of ZGNRs. U-shaped precursor is designed for the synthesis of 6-ZGNR upon polymerization (step 1) and subsequent cyclodehydrogenation (step 2). (B) Constant height nc-AFM image of 6-ZGNR with a CO-functionalized tip. Scale bar, 1 nm. (C) STM image of a 6-ZGNR segment transferred onto monolayer NaCl islands via tip manipulation. Scale bar, 2 nm. (D) Calculated quasiparticle band structure (energy versus wave vector  $k$ ) (left, black;  $a$  is the lattice parameter) and density of states (DOS, right, grey) for an infinitely long 6-ZGNR. (E)  $dI/dV$  spectrum (red) taken at the zigzag edge as marked by the red circle in (C) and the calculated quasiparticle DOS (grey). (F)  $dI/dV$  maps of filled (left) and empty (right) edge states taken at the sample bias of  $-0.3$  V and  $1.0$  V, respectively. (G) DFT-calculated LDOS maps of filled (left, with overlaid structural model) and empty (right, with overlaid structural model) edge states. Scale bar is 1 nm. Reproduced with permission from ref. 15. Copyright 2016 Nature publishing group.

larger precursors that usually suffer from low solubility and high sublimation temperature, which poses additional challenge for on-surface synthesis of wider ZGNRs. As an alternative to the bottom-up approach, Magda *et al.* developed a nanolithography method for the fabrication of wide ZGNRs by cutting graphene sheet into sub-nanometer-wide channel using STM tip under ambient conditions.<sup>109</sup>  $dI/dV$  measurements in combination with theoretical calculations reveal a semiconductor-to-metal transition when the width of ZGNRs increases above 8 nm. The experimental observation of a steep antiferromagnetic (semiconductor) to ferromagnetic (metal) transition can be explained within mean-field approximation of the Hubbard model including the temperature and doping effects.

It has been reported that wide AGNRs can be formed by side-by-side inter-chain fusion of narrow GNRs via an intermolecular dehydrogenation reaction.<sup>110–113</sup> This strategy was adopted by Beyer *et al.* for the synthesis of zigzag edge-expanded GNRs (zeeGNRs) with a higher ratio of zigzag edge (67%) as compared to armchair edge (25%).<sup>114</sup> Although all the zeeGNRs with different widths show a closed-shell ground state, it provides a new approach for the synthesis of open shell GNRs in the future.

Although localized edge states were found in the above-mentioned ZGNRs, the long-predicted magnetism of these structures was not directly resolved. In contrast, magnetic response has been established in specific sites of localized spins hosted by certain recently reported GNR junctions. Li *et al.* observed that single spin localization can emerge at some specific sites in the junction of two chiral GNRs via the detection of Kondo resonances (Fig. 7A and B) and spin-excitation gaps (Fig. 7E).<sup>16</sup> The junction structures were synthesized on Au(111) by cross-dehydrogenative coupling of adjacent GNRs with the same chirality. The formation of a stable junction structure involves a reorganization of carbon atoms around the initial contact point. Spin density is located at the pentagon cove site and terminal zigzag site of the junctions. STS measurements of the Type 1 and Type 2 junctions reveal pronounced zero-bias peaks arising from the Kondo effect. The characteristic temperature-dependent (Fig. 7C) and magnetic field-dependent (Fig. 7D) behaviors further support the assignment of zero-bias feature as Kondo resonance. The Fano line shape of the Kondo resonance originates from the quantum interference between two tunnelling channels including (i) through the vacuum and (ii) through the atom/molecule. An enhanced tunnelling through the atom/molecule with the suppressed tunnelling through the vacuum gives rise to the Lorentzian peak feature, while it appears as a dip if the tunnelling through the vacuum is dominated over the tunnelling through the atom/molecule.<sup>115,116</sup> Therefore, a dip often appears over the single magnetic adatoms (*i.e.* Co, Fe, *etc.*) and metal-molecule complexes (*i.e.* CoPc, FePc, *etc.*) with more localized magnetic moment on metal surfaces.<sup>117,118</sup> In addition, the Fano line shape of Kondo resonance also depends on their specific adsorption site that affects the tunnelling probability through different channels.<sup>117,118</sup> However, the spin density in open-shell GNs is often delocalized around/above a nanometre range in the  $\pi$ -conjugated lattice. It is expected that the delocalization of spin density over a large space region in the open-shell GNs disfavours the tunnelling through the vacuum, leading to the emergence of Lorentzian peak feature.

$dI/dV$  spectra taken over Type 3 junctions at the terminal zigzag segment and pentagon cove regions show step-like features (at  $\pm 10$  meV) in the vicinity of Fermi level (Fig. 7E). Such a symmetric step feature across Fermi level in  $dI/dV$  spectra was attributed to the excitation of two exchange coupled spins localized at the junction site by tunneling electrons. Moreover, the spin exchange coupling strength increases with the length of the connecting ribbons (Fig. 7F).



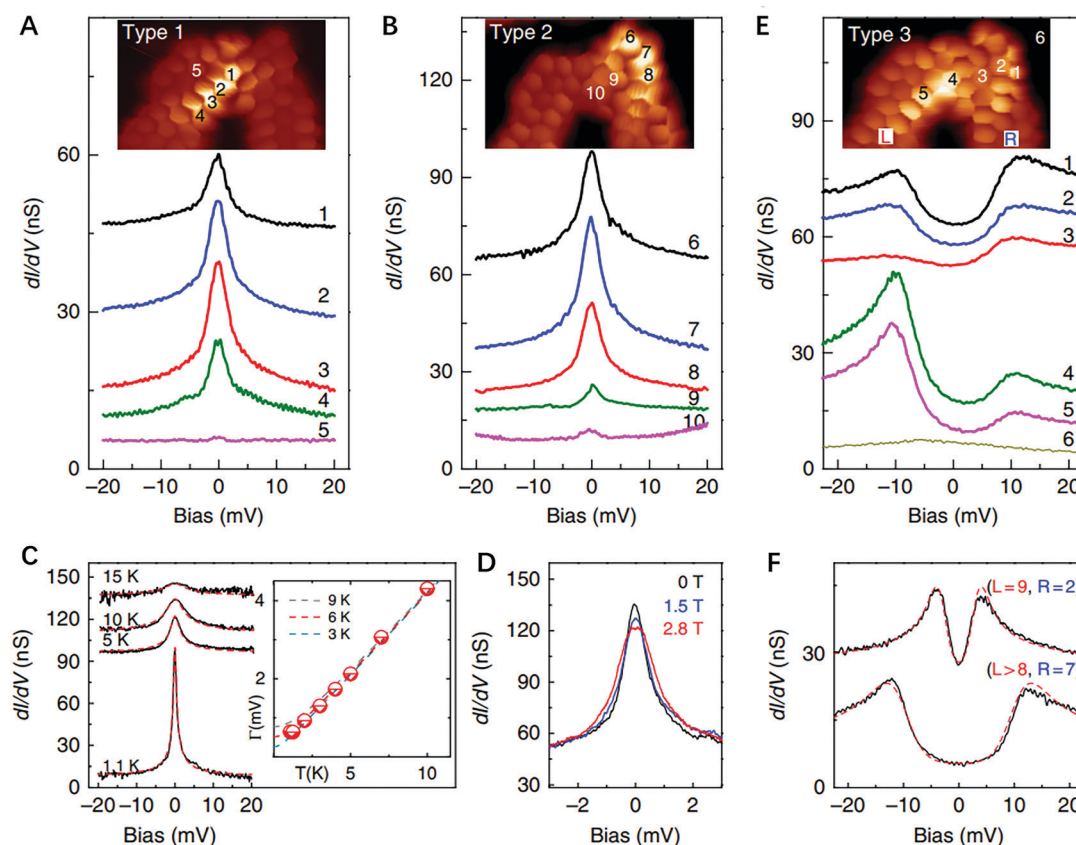


**Fig. 7** On-surface fabrication and characterization of GNR junctions from (3,1)chiral GNRs. (A and B) Kondo resonances over the bright regions of Type 1 and Type 2 junctions, respectively (insert is the BRSTM image of the corresponding junction). (C) Temperature dependence of Kondo resonance (black lines) with Frota function fitting (red dashed lines) of  $dI/dV$  spectra taken over the pentagon cove site. Inset shows the Fermi-liquid fit of the extracted HWHM at each temperature. (D) Magnetic field dependence of a Kondo resonance (over the same pentagon cove site). (E) The spin-excitation features around zero bias over Type 3 junctions. (F) Spin excitation gaps of the junctions with different sizes, determined by the precursor unit number in each junction, labelled as L and R in (E). Reproduced with permission from ref. 16. Copyright 2016 Nature publishing group.

#### 4.4 Zigzag termini of AGNRs

The zigzag edge geometry can be also generated on the termini of AGNRs *via* bottom-up on-surface synthesis. Although various atomic structures can be found at the termini of AGNRs, our discussion focuses on the ones with monohydrogen-terminated zigzag ends.<sup>119–121</sup> There has been a long debate on the nature of end states of the short zigzag termini of AGNRs. Earlier theoretical work predicts that these end states are spin polarized.<sup>120</sup> In contrast, Møller-Plesset perturbation theory incorporating the electron correlation effect indicates that such edge states are pseudo-spin polarized. This has been discussed by Huzak *et al.*<sup>122</sup> and more recently by Aristides.<sup>123</sup>

Recently, the end states localized at the zigzag termini of 5-AGNR<sup>121</sup> and 7-AGNR<sup>119</sup> have been characterized by STM. James *et al.* has investigated the electronic structure of several 5-AGNRs with different lengths adsorbed on Au(111) and monolayer NaCl islands, respectively. High resolution STM image resolves the backbone of the ribbon, while constant-height  $dI/dV$  maps reveal its three electronic states located at 700 mV, 137 mV and –150 mV, respectively (Fig. 8A).  $dI/dV$  mapping reveals that the in-gap state at 137 mV is confined to the end regions, while the states at –150 mV and 700 mV are

associated with the valence band and conduction band onsets, respectively. The magnetic character of the end states was demonstrated *via* transport measurement by lifting up GNR using STM tip. The conductance of the ribbons is measured as a function of the lifting height (Fig. 8B). The observation of a Kondo resonance (Fig. 8B) proves the magnetic nature of the ribbon terminals. In addition, the magnetic end states of the GNR quench as evidenced by the disappearance of Kondo resonance upon its exposure to molecular oxygen.

STM manipulation can be used to transfer as-grown GNRs from the metallic substrate onto insulating NaCl islands to electronically decouple GNRs from the metal.<sup>124</sup> Wang *et al.* reported the study of the zigzag termini of a series of (7,*n*) AGNRs, where *n* represents the lateral dimension along the armchair direction in the unit of carbon zigzag lines.<sup>119</sup> In the study, GNRs with different lengths (ranging from 3 to 10 nm) were moved onto NaCl islands to probe the electronic coupling between the end states as a function of ribbon length. Fig. 8A–D shows the STM images (upper panel) and  $dI/dV$  maps (lower panel) of the empty and filled edge states of (7,12), (7,16), (7,20) and (7,48) GNRs on NaCl islands. It was found that the end states are localized near the zigzag termini (Fig. 8A–D).

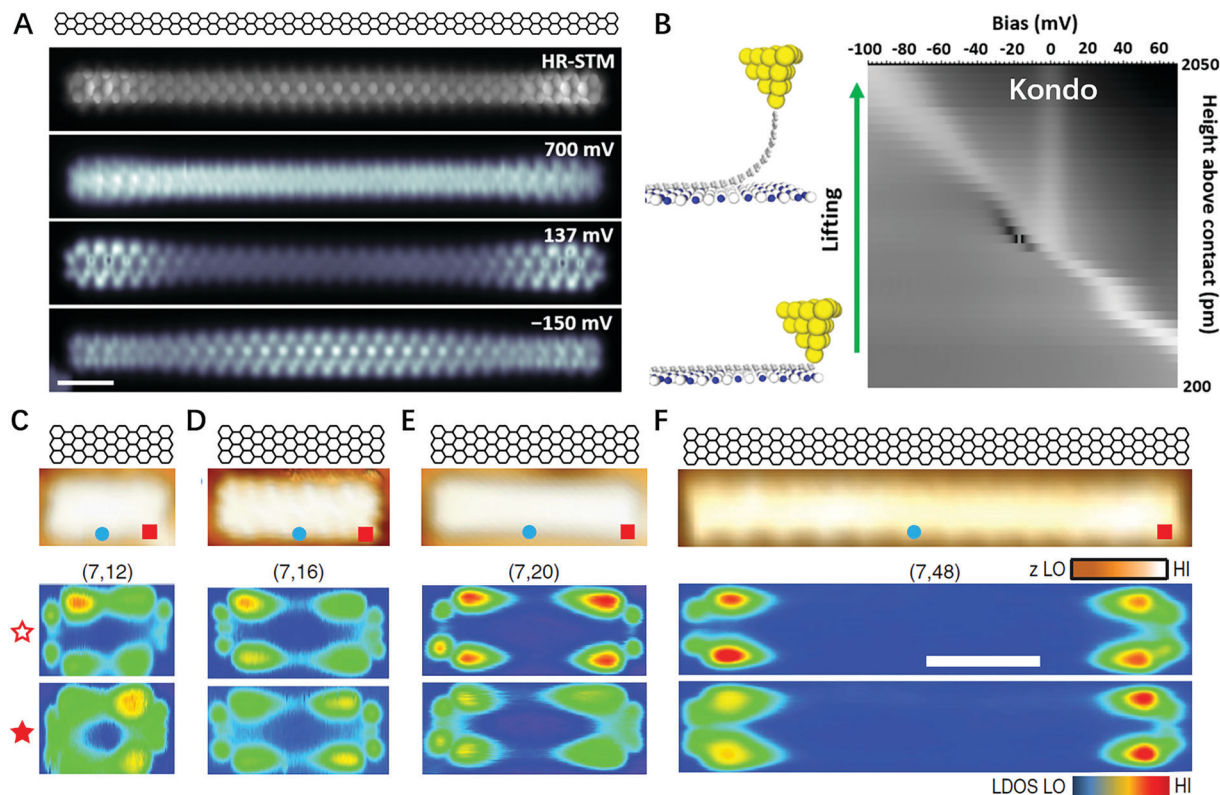


**Fig. 8** Characterization of the zigzag terminals of armchair-edged GNRs. (A) High resolution STM image of a 5-AGNR and constant height  $dI/dV$  maps of three states near the Fermi level. (B) 2D conductance map of  $dI/dV$  spectra during lifting the GNR over NaCl island measuring transport. Zero-bias Kondo feature is observed due to localized magnetic moment at the terminal. (C–F) STM topography images and  $dI/dV$  maps of empty and filled edge states of decoupled (7,12), (7,16), (7,20) and (7,48) GNRs on monolayer NaCl islands ( $-0.1$  V, 30 pA). Reproduced with permission from ref. 119 and 121. Copyright 2016 Nature publishing group, 2020 American chemical society.

The fundamental gaps of these GNRs were determined by the energy splitting  $\Delta_{zz}$  between the occupied and empty end-localized states. Over the length range of 3–10 nm of the AGNRs,  $\Delta_{zz}$  is essentially independent of the separation between the zigzag edges, in accordance with the GW predictions. In contrast, the bulk band gap  $\Delta_{AC}$  decreases continuously from 3.5 eV for the shortest (7,12) GNR to 2.9 eV for the longest (7,48) GNR. This trend is rationalized by a reduced longitudinal confinement of the associated bulk states that extend throughout the whole AGNR.

#### 4.5 [n]Triangulenes and [7]triangulene quantum ring

The extension of fused benzene rings in a triangle fashion along the zigzag crystallographic direction leads to a series of open-shell zigzag-edged triangular graphene molecules (ZTGMs), namely, [n]triangulene series ( $n$ : the number of benzenoid rings along each zigzag edge, Fig. 9A).<sup>51,96,103</sup> The unique topology of these molecules makes it impossible to construct their Kekulé-style resonance structures without leaving unpaired electrons. Therefore, these molecules are regarded as non-Kekulé polynuclear benzenoids, whose total net spin can be quantified based on the Ovchinnikov's rule established by Lieb's theorem for bipartite lattices. According to this rule, the ground-state spin quantum number of GNs is

determined by  $S = \frac{(N_A - N_B)}{2}$ , where  $N_A$  and  $N_B$  denote the number of carbon atoms from the two interpenetrating triangular sublattices, respectively (marked by blue and orange circles in Fig. 9A). The progress on the synthesis and characterization of a series of ZTGMs has been covered in our previous mini-review, which will not be discussed in details here.<sup>125</sup> Instead, we would like to highlight the recent advance in the synthesis of triangulene quantum rings (TQRs).<sup>126</sup>

Topological engineering *via* creating an antidot in large triangulene homologues provides an alternative approach to fabricate a series of intriguing TQRs with a tunable spin quantum number and magnetic ordering.<sup>127,128</sup> In particular, the spin-polarized energy gap and spin density distribution of TQRs can be precisely controlled *via* tailoring the topology of antidots in TQRs. Similar to triangulenes, the ground-state spin-quantum number of TQRs can be predicted by Ovchinnikov's rule. As illustrated in Fig. 9B, the removal of a coronene-moiety from a [7]triangulene leads to the formation of a [7]TQR molecule with a hexagonal antidot in the center. It is noted that the removed coronene-motif contains an equal number of each sublattice so that both [7]TQR and [7]triangulene counterpart share the same ground-state spin quantum number ( $S = 3$ ).

In order to demonstrate the concept of antidot engineering, we designed a new molecular precursor with a kekulene core as

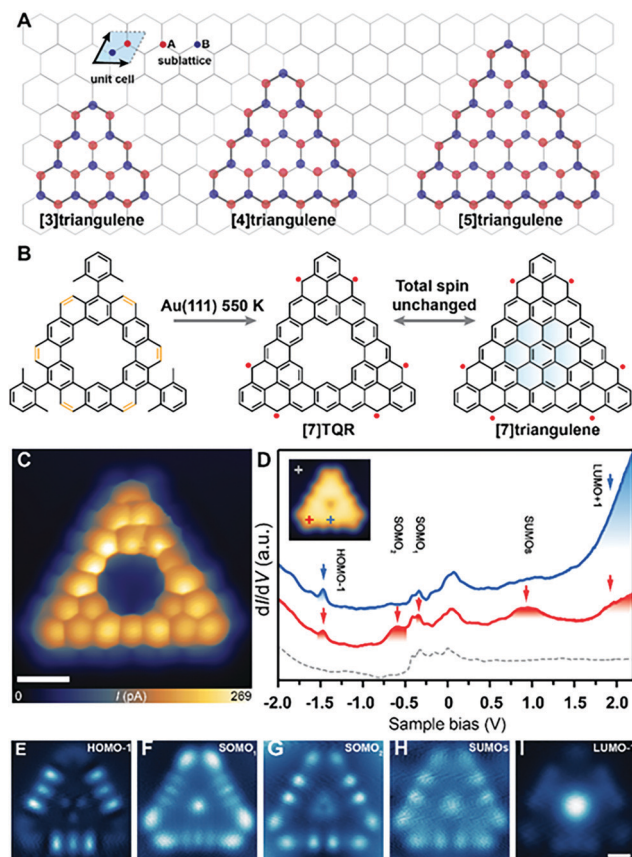


**Fig. 9**  $[n]$ triangulene series and [7]triangulene quantum ring ([7]TQR). (A) Atomic structure with labelled sublattices of [3]triangulene, [4]triangulene, and [5]triangulene, respectively. Blue and orange circles denote carbon atoms belong to different sublattice in a graphene unit cell. (B) Schematic illustration of the synthesis of [7]TQR and antidot engineering. The total spin of [7]TQR remains unchanged after introducing a hexagonal anti-dot in [7]triangulene. (C) BR-STM image of a [7]TQR molecule synthesized on Au(111). (D) Point  $dI/dV$  spectra acquired over different sites of [7]TQR and Au(111). (E–I) Constant-current  $dI/dV$  maps recorded at different energy positions corresponding to different molecular states marked by red and blue arrows in (D). Reproduced with permission from ref. 126. Copyright 2020 American Chemical Society.

shown in Fig. 9B. The annelated macrocyclic topology of the kekulene and other cycloarenes makes them as the promising candidates for the synthesis of atomically-precise TQRs *via* antidot engineering. The attached three 2,6-dimethylphenyl substituents undergo the surface-assisted cyclodehydrogenation with the adjacent carbon atoms at elevated temperatures under ultra-high vacuum (UHV) conditions, forming the well-defined [7]TQR. BR-STM imaging of as-synthesized [7]TQR reveals its characteristic zigzag edge topology along with a hexagonal hole in the molecular center (Fig. 9C).  $dI/dV$  spectroscopic measurements and spin-polarized density functional theory (DFT) calculations were performed to unveil its spin-polarised electronic structures. Among all the magnetic configurations, ferromagnetic septuple state ( $S = 3$ ) is predicted to be the most energetically favourable.  $dI/dV$  spectrum acquired at the corner and the edge positions reveal several features located at  $-0.3$  V,  $-0.61$  V and  $+0.91$  V (Fig. 9D), which can be ascribed

to the singly occupied molecular orbitals (SOMO<sub>1</sub>), (SOMO<sub>2</sub>) and singly unoccupied molecular orbitals (SUMOs), respectively. An energy separation of  $\sim 300$  meV between SOMO<sub>1</sub> and SOMO<sub>2</sub> is due to a lower degree of degeneracy of SOMOs as predicted by spin-polarized DFT calculations. Besides, the experimental  $dI/dV$  maps show an edge-localization of the SOMOs and SUMOs (Fig. 9F–H). In addition, pronounced contrast of the  $dI/dV$  map in the center of the [7]TQR, indicating the HOMO–1 and LUMO+1 are localized at the inner edges of the [7]TQR (Fig. 9E and I). All these observations manifest that the septuple magnetic ground states ( $S = 3$ ) of [7]TQR is retained on Au(111). The successful synthesis of TQR *via* antidot engineering opens up a new avenue for the fabrication of high-spin graphene quantum nanostructures towards next-generation quantum devices.<sup>6</sup>

#### 4.6 Triangulene dimers

Connecting two triangulene units *via* their tips (the minority sublattice atoms) forms a triangulene dimer without sublattice imbalance, which is thus expected to be a low-spin ground state of  $S = 0$ .<sup>129</sup> Introducing a phenyl ring as an organic spacer to join two triangulene molecules not only tunes the magnetic coupling between two triangulene units but also modifies their magnetic correlations (Fig. 10A). Fig. 10B and C present the chemical structures of designed precursors with the corresponding synthetic strategies towards the formation of triangulene dimers with and without a 1,4-phenylene spacer on Au(111). High-resolution STM images reveal their molecular geometries with the lobed patterns of these two different dimers, while Laplace-filtered bond-resolved STM (BRSTM) images (Fig. 10D) resolve their molecular backbones at the single-bond level.

MFH model including electron–electron correlations reveals the formation of SOMOs and SUMOs with a sizeable Coulomb gap. It also suggests that individual triangulene units in two dimers are antiferromagnetically coupled, leading to an open-shell singlet ground state ( $S = 0$ ). The MFH spin density distribution of two dimers are shown in Fig. 10E.  $dI/dV$  spectra taken on two dimers reveal broad peaks centered at about  $-400$  mV and  $+1.25$  V (Coulomb gaps of these two dimers are approximately equal 1.65 eV), which confirm the formation of the spin-split frontier molecular orbitals of both molecules.  $dI/dV$  spectrum taken on the triangulene dimer without a spacer reveals a symmetric step-like feature in the vicinity of  $E_F$ , which is attributed to the singlet-to-triplet ( $S = 0$  to  $S = 1$ ) spin excitation with an excitation threshold of  $\pm 14$  mV. Similarly, the  $dI/dV$  spectrum acquired on triangulene dimer with a 1,4-phenylene spacer also presents a singlet–triplet spin excitation with a substantially-reduced excitation threshold of  $\pm 2$  mV. These results indicate that the inter-triangulene magnetic coupling can be tuned with the spatial separation between the triangulene units.

#### 4.7 Extended triangulenes and Clar's goblet

The magnetism induced by the sublattice imbalance also exists in one of the extended triangulenes (ETRI) as shown in Fig. 11A. This extended triangulene processes 19 carbon atoms in one



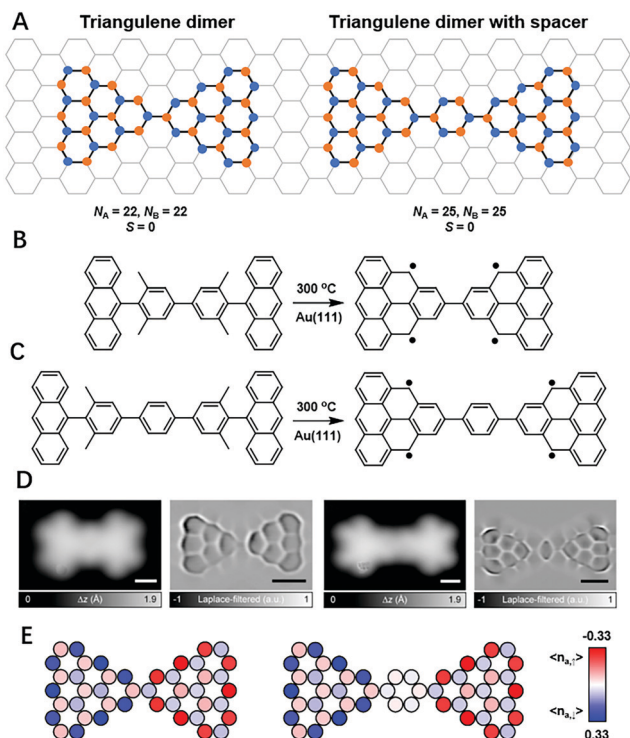


**Fig. 10** On-surface synthesis of triangulene dimers. (A) Atomic structure of triangulene dimer and triangulene dimer connected with a 1,4-phenylene spacer. Blue and orange circles denote carbon atoms belong to different sublattice. (B and C) Schematic illustration of the precursor and on-surface synthesis of (B) triangulene and (C) triangulene dimer with a 1,4-phenylene spacer, respectively. (D) High-resolution STM images with the corresponding Laplace-filtered BRSTM images of the triangulene dimer and triangulene dimer with a 1,4-phenylene spacer. Scale bars in panel D are 0.5 nm. (E) MFH spin polarization plots of the triangulene dimer (left) and triangulene dimer with a 1,4-phenylene spacer (right). Reproduced with permission from ref. 126. Copyright 2019 John Wiley and Sons.

sublattice and 17 carbon atoms in the other, resulting in a total spin  $S = 1$  according to Lieb's theorem (Fig. 11A).<sup>130</sup> This is in contrast to the double triangulene (DTRI) without sublattice imbalance (Fig. 11A).

The synthetic strategies for ETRI and DTRI molecules are depicted in Fig. 11B. The constant height current image with a CO-functionalized tip resolves the molecular backbone structure for both ETRI (Fig. 11C) and DTRI (Fig. 11E). It is noted that ETRI shows additional bright features at the edges for the STM image recorded at 2 mV, which indicates an enhanced LDOS at these specific sites close to  $E_F$ . Such a difference is further manifested by the  $dI/dV$  spectra measured on both structures. ETRI shows a pronounced zero-bias peak in the  $dI/dV$  spectrum, which can be attributed to the Kondo effect arising from the screening of local spin by conduction electrons. The assignment of zero-bias feature as Kondo resonance is further supported by its characteristic temperature-dependent (Fig. 11F) and magnetic field-dependent (Fig. 11G) behaviors. The zero-bias peaks get broadened as temperature increases. A plot of the half width at half maximum (HWHM) of zero-bias peak *versus* temperature follows the trend as

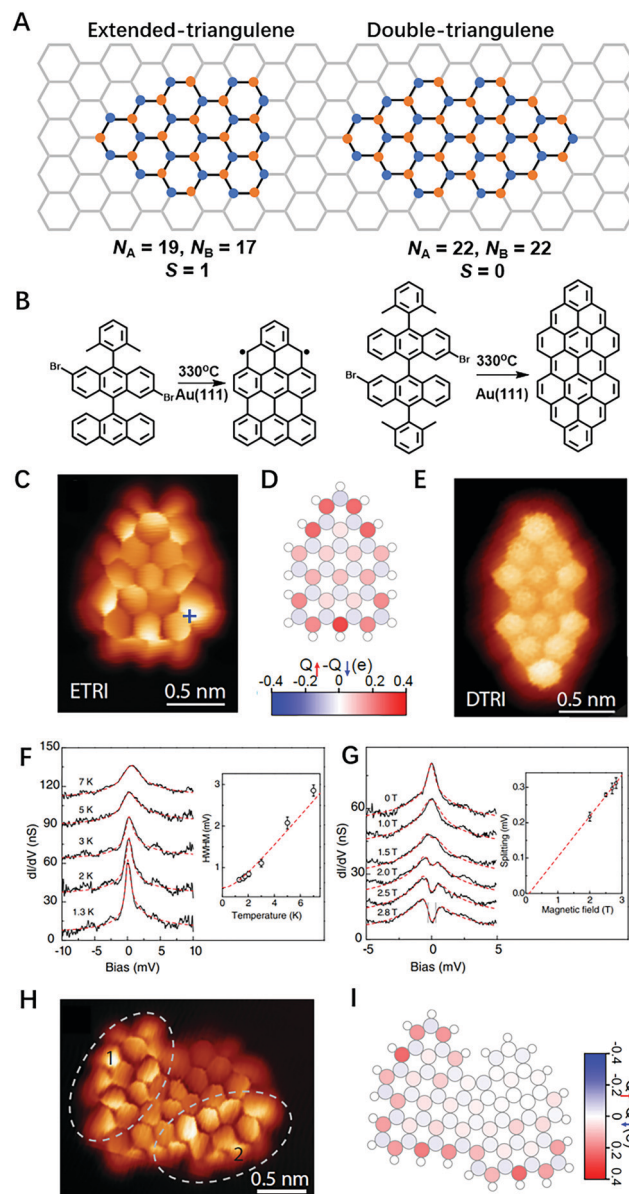


**Fig. 11** On-surface synthesis of extended triangulene. (A) Atomic structure of ETRI and DTRI molecules. Blue and orange circles denote carbon atoms from two sublattices. (B) Synthetic routes toward the fabrication of ETRI (left) and DTRI (right). Bond-resolved STM images of (C) ETRI, (E) DTRI and (H) ETRI dimer. MFH spin polarization maps of (D) ETRI and (I) ETRI dimer. (F) Temperature dependence of Kondo resonance for the ETRI molecule (measured at the site marked by blue cross in (C) with Frota function fitting (red dashed lines)). The inset plots the half width at half maximum (HWHM) at each temperature with Fermi-liquid fitting result of Kondo temperature  $T_K \sim 6$  K. (G) Magnetic field dependence of the Kondo resonance with fitting curves (red dashed lines). The inset shows the dependence of Zeeman splitting ( $g = 1.98 \pm 0.07$ ) of the Kondo resonance with magnetic fields. Reproduced with permission from ref. 130. Copyright 2019 American Physical Society.

predicted by Fermi-liquid model (Fig. 11F inset), which yields a Kondo temperature of  $T_K \sim 6$  K. Furthermore, the zero-bias peaks show a characteristic Zeeman splitting as magnetic field increases. A linear fit of the splitting energy as a function of magnetic field (Fig. 11G inset) gives rise to the Landé factor of

$g = 1.98 \pm 0.07$ , close to the value for a free electron ( $g_0 = 2$ ). These additional evidences further confirm that the zero-bias peak can be assigned as Kondo resonance, which therefore offer a direct proof of magnetic response of the open-shell ETRI on Au(111). By contrast, the  $dI/dV$  spectrum of DTRI is rather featureless in the vicinity of  $E_F$ , suggesting a closed-shell ground state. Mean-field Hubbard (MFH) calculations also reveal an emergence of magnetism in ETRI with a ferromagnetic (open-shell triplet) ground state. Two spin centers of ETRI are predicted to localize at opposite sides of the trianguleneoid (Fig. 11D), which resembles the experimental current map (Fig. 11C).

A paramagnetic ground state was also observed for molecular dimers formed during the annealing process (Fig. 11H). Two

ETRI moieties are covalently linked through the Ullmann-like C-C coupling *via* the halogenated sites to form an extra pentagonal ring between two monomers. The current map acquired at 2 mV (Fig. 11H) reveals the bright features around the dimer backbone well (indicated by the dashed ellipses) corresponding to the localization of the Kondo resonance (the  $dI/dV$  spectra measured on either of the two show a prominent zero-bias peak). The spin polarization maps obtained from MFH simulations reproduce the bright features in the current map well (Fig. 11I).

Shantanu *et al.* fabricated a linearly-fused dimer of ETRI (denoted as LDETRI, Fig. 12A).<sup>131</sup> BRSTM images of LDETRI (Fig. 12B and C) confirm its all-benzenoid topology with triangulene-like termini. The calculated spin density distribution

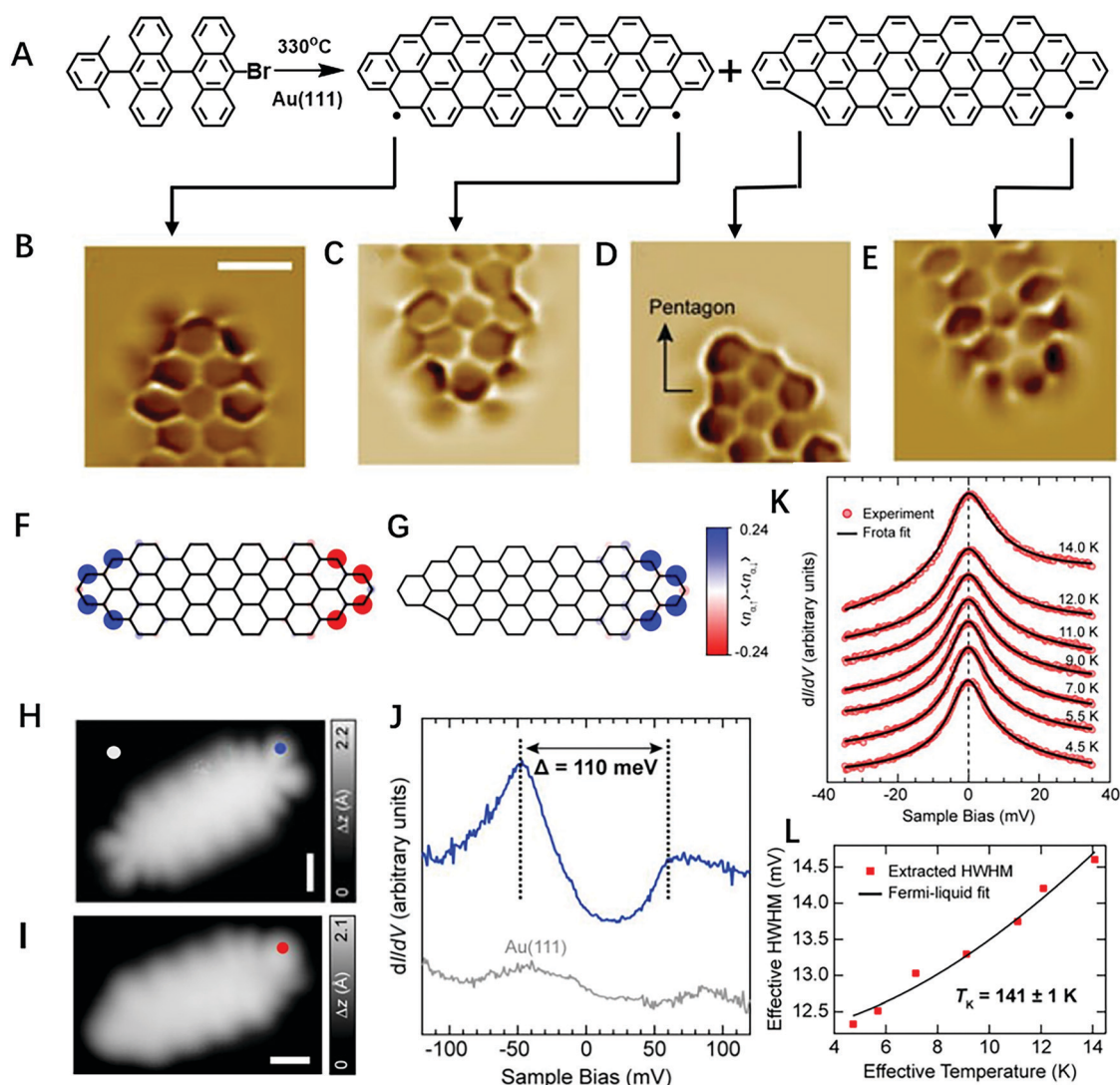


**Fig. 12** On-surface synthesis of LDETRI and LDETRI with pentagon ring. (A) Illustration of the synthetic route toward the formation of LDETRI and LDETRI with a pentagon ring. (B–E) Laplace-filtered BRSTM images of the termini of LDETRI (B and C) and LDETRI with a pentagon ring (D and E). Scale bar is 0.5 nm. Tunneling parameters:  $V = -5$  mV,  $I = 50$  pA. (F and G) MFH spin density distribution of LDETRI (F) and LDETRI with a pentagon ring (G). Blue/red isosurfaces denote spin-up/spin-down density. (H and I) STM image of LDETRI (H) and LDETRI with a pentagon ring (I). Scale bars in H and I are 0.5 nm. (J)  $dI/dV$  spectrum of LDETRI. The position where  $dI/dV$  spectrum was acquired is marked with blue circle in (H). (K) Temperature dependence of the Kondo resonance with Frota fitting detected at the position marked by red dot in (I). (L) Temperature dependent of the extracted HWHM of the Kondo resonance, with Fermi-liquid fitting. Reproduced with permission from ref. 131. Copyright 2019 American Chemical Society.

of LDETTRI (Fig. 12F) within MFH model reveals the dominant spin localization at the zigzag carbon atoms of the termini, with the spatial separation of spin up and spin down populations. The  $dI/dV$  spectrum (Fig. 12J) taken at the triangulene-like termini (Fig. 12H) reveals two peaks at  $-50$  mV and  $+60$  mV in the vicinity of  $E_F$ , yielding a frontier electronic gap of 110 meV.

Interestingly, the majority of the products (94%) exhibit different STM contrast at two termini (denoted as LDETTRI with a pentagon ring). While one terminus presents a two-lobed feature similar to that of LDETTRI, the other terminus exhibits a triangular topography without two-lobed feature (Fig. 12I). BRSTM images of LDETTRI with a pentagon ring (Fig. 12D and E) reveal the formation of a pentagonal ring in the left terminus and a retained triangulene-like pattern of the right terminus. The formation of a pentagon ring results from the loss of a single methyl group from an Ullmann-coupled dimer. Notably, an enhancement of zero-bias LDOS occurs exclusively on the triangulene-like terminus. In contrast to the all-benzenoid topology, the presence of a pentagon disrupts the bipartite symmetry of the underlying honeycomb lattice, and thus Ovchinnikov's rule cannot be applied to determine the ground

state spin multiplicity. As a result, a non-Kekulé structure is formed with an unpaired electron ( $S = \frac{1}{2}$ ). The calculated spin density distribution of the molecule reveals a spin localization only at the triangulene-like terminus. The  $dI/dV$  spectrum performed on that terminus (red circle labeled in Fig. 12I) also reveals a zero-bias peak whose temperature-dependent half width at half maximum (HWHM) follows the characteristic broadening trend of a Kondo resonance (Fig. 12K) and can be fit with Femi-liquid model (Fig. 12L).

Despite the absence of sublattice imbalance, certain benzenoid topologies have been hypothesized to be open-shell non-Kekulé GNs. Shantanu *et al.* recently reported a bowtie-shaped GN, namely Clar's goblet with antiferromagnetic (open-shell singlet) ground state (Fig. 13A). It was first envisioned by Erich Clar<sup>132</sup> in 1972 that topological frustration in the  $\pi$ -electron network renders it impossible to assign a classical Kekulé structure without leaving unpaired electrons, driving the system into a magnetically non-trivial ground state.

Fig. 13B depicts the synthetic strategy of the Clar's goblet,<sup>113</sup> wherein the methyl groups connected to the central benzene ring serve as pre-selected reactive sites that are expected to

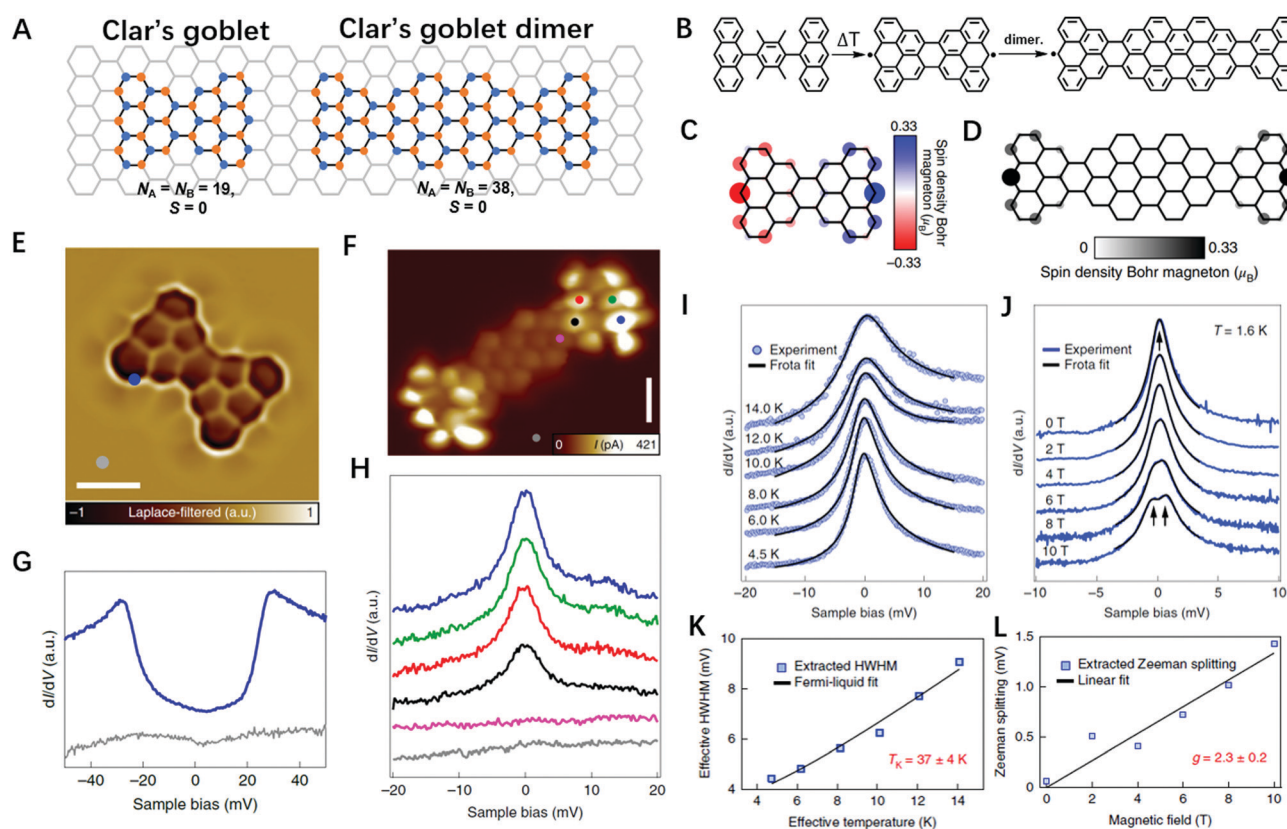


**Fig. 13** On-surface synthesis of Clar's goblet and its dimer. (A) Illustration of the atomic structure of Clar's goblet and Clar's goblet dimer. Blue and orange circles denote carbon atoms belong to different sublattices. (B) Synthetic routes of Clar's goblet and its dimer. (C and D) MFH spin density distribution of Clar's goblet and Clar's goblet dimer. Spin up/spin down density are represented in different colors. (E and F) Laplace-filtered BRSTM images of Clar's goblet and Clar's goblet dimer. Scale bars in E and F are 0.5 nm. (G)  $dI/dV$  spectrum of Clar's goblet measured at the site indicated in (E). (H)  $dI/dV$  spectra acquired in the vicinity of EF over the Clar's goblet dimer at different sites of the terminal triangular motif indicated in (F). (I and J) Temperature and magnetic field dependent Kondo resonance with Frota function fit. (K) Extracted HWHM of the Kondo resonances as a function of temperature, with corresponding fit using the Fermi-liquid model. (L) Zeeman splitting of the Kondo resonance as a function of magnetic field, with corresponding linear fit. Reproduced with permission from ref. 113. Copyright 2020 Nature Publishing Group.



undergo surface-catalyzed oxidative ring closure against the anthracene moieties to form the target product. BRSTM image (Fig. 13E) with a CO-functionalized tip confirms the successful formation of the desired product.

The electronic structure of the molecule was characterized *via*  $dI/dV$  spectroscopy. A series of peaks are observed at  $-1.15$  V,  $-300$  mV,  $+1.00$  V,  $+1.80$  V and  $+2.20$  V, which can be assigned to HOMO-1, SOMO, SUMO, LUMO+1 and LUMO+2, respectively. The Coulombic gap is determined to be  $1.30$  eV on the basis of the energies of the SOMO and SUMO resonances. Fig. 13C shows the spin density distribution of Clar's goblet. The spin up and spin down populations are sublattice-polarized and localized on opposite parts of the molecule, thus maintaining a local spin polarization. In addition,  $dI/dV$  spectrum acquired in the vicinity of the  $E_F$  over this molecule shows symmetric step-like features at  $\pm 23$  mV, attributed to the singlet-triplet spin excitations.<sup>133</sup> The delocalized nature of  $\pi$ -radical renders the molecule with sufficient stability to prevent spin quenching on the metallic substrate. The broad peak profile of the spin excitation spectrum indicates a finite Kondo coupling of individual spins with surface electrons.<sup>134</sup>

The spectroscopic analysis above confirms that the two spin centers are coupled anti-ferromagnetically with an exchange-coupling strength of  $J_{\text{eff}} = 23$  meV. A further increase of the separation of the spin-bearing moieties is expected to decouple the interaction between two spin centres ( $J_{\text{eff}} = 0$ ), wherein individual spins behave as free paramagnetic centres ( $S = \frac{1}{2}$ ). Therefore, screening of individual spins by itinerant conduction electrons on the surface results in many-body Kondo ground state. This scenario can be realized by a linear fusion of two Clar's goblet molecules to generate a dimer (Fig. 13B).  $dI/dV$  spectroscopic measurements reveal that a zero-bias peak (Fig. 13H) can be observed at the terminal triangular motif but is absent in the center of the dimer. In addition, this zero-bias peak shows a characteristic temperature-dependent linewidth broadening (Fig. 13I) and magnetic-field dependent peak splitting (Fig. 13J) that follows the expected behaviors of Kondo resonance. The Fermi-liquid fitting result of the extracted HWHM yields a Kondo temperature of  $T_k = 37 \pm 4$  K (Fig. 13K), and the linear fitting of the extracted Zeeman splitting generates a  $g$  factor of  $2.3 \pm 0.2$ . The calculated spin density distribution of the dimer (Fig. 13D) reveals a negligible spin density at the central part of the molecule, consistent with the spatial intensity distribution of Kondo resonance.

#### 4.8 Rhombenes

On-surface synthesis of ZGNs with a rhombus shape, namely  $[n]$ -rhombenes, where  $n$  is the number of benzenoid rings along an edge, has been reported recently by Shantanu and co-workers.<sup>135</sup> The  $[n]$ -rhombenes with balanced sublattice are expected to possess singlet ground state with a total spin quantum number  $S = 0$  (Fig. 14A). The precursor design and synthetic strategy of [4]-rhombene and [5]-rhombene are shown in Fig. 14B and C, respectively. Theoretical calculations revealed that  $[n]$ -rhombenes gradually acquire an open-shell singlet ground state when  $n$  is larger than 5 (closed-shell for  $n \leq 4$  and open-shell

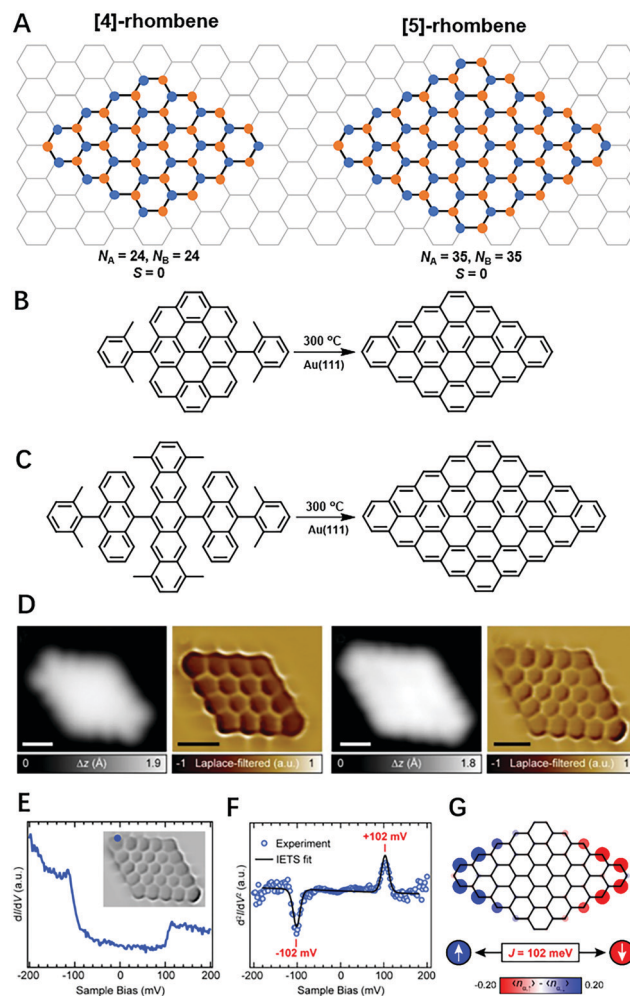


**Fig. 14** On-surface synthesis of rhombenes. (A) Atomic structure of [4]-rhombene and [5]-rhombene. Blue and orange circles denote carbon atoms belong to different sublattices. (B and C) Schematic illustration of the precursor and on-surface synthesis of (B) [4]-rhombene and (C) [5]-rhombene respectively. (D) High-resolution STM and Laplace-filtered BRSTM images of [4]-rhombene and [5]-rhombene. Scale bars in D are 0.5 nm. (E)  $dI/dV$  spectrum acquired over the corner of [5]-rhombene as marked by filled blue circle in the inset. (F) The corresponding IETS spectrum (filled circles), and fitted curve using the Heisenberg dimer model (solid line). The spin excitation threshold is extracted to be  $\pm 102$  mV. (G) Mean-field Hubbard spin polarization plot of the open-shell singlet ground state of [5]-rhombene with schematic illustration of the exchange coupling of spins. Blue and red isosurfaces denote spin up and spin down populations. Reproduced with permission from ref. 135.

for  $n \geq 5$ ). In this system, Coulomb repulsion triggers the spin polarization, attributed to the magnetism. In addition, theory prediction suggests that low-energy spin-localized states of GNs shift towards Fermi level as their size increases.<sup>7,8</sup>

BRSTM images (Fig. 14D) ambiguously reveal the backbone of both [4]-rhombene and [5]-rhombene molecules whose electronic structures are probed by  $dI/dV$  spectroscopy.  $dI/dV$  spectrum of [4]-rhombene, shows two peaks located at  $-330$  mV and  $400$  mV, which can be assigned to close-shell HOMO and LUMO orbitals as supported by DFT calculations. In contrast,  $dI/dV$  spectrum of [5]-rhombene reveals a symmetric

step-like feature around  $E_F$  due to spin excitation (Fig. 14E). The excitation threshold was measured to be  $\pm 102$  meV *via* the fitting of experimental IETS spectrum to the Heisenberg dimer model (Fig. 14F). Spin-polarized DFT calculation of the magnetic ground state of the [5]-rhombene further confirms that the inelastic excitation can be ascribed to the spin excitation in this system. Fig. 14G presents the MFH spin polarization maps of [5]-rhombene, wherein spin up and spin down electrons are populated at sublattice-polarized sites localized at the opposite ends of the molecule.

#### 4.9 Circumcoronene

Hexagonal GNs with six zigzag edges (namely  $[n]$ coronene, where  $n$  is the number of carbon atoms in each zigzag edge.) were predicted to show open-shell ground state as the size increases to a certain regime. For example, the [2] and [3]coronene are predicted to be closed-shell, while a larger [4]coronene shows an open-shell multiradical character.<sup>7</sup> The synthesis of large-sized coronene homologues represents a big challenge due to their high chemical reactivity, which thus call for a rational design and synthesis of the large elegant precursors for on-surface synthesis.

Recently, we reported a novel surface-assisted synthetic route for an ultra-high yield fabrication of circumcoronene and its superlattice on Cu(111).<sup>136</sup> Specifically, we designed a unique precursor molecule, which consists of coronene core attached by the corner benzene rings decorated with six pairs of methyl groups (Fig. 15A). Such a precursor design prevents the undesired intramolecular and intermolecular side reactions, thereby allows for a high-yield ( $>98\%$ ) synthesis of circumcoronene. The chemical transformation of precursor molecule into circumcoronene involves two major steps, namely the dehydrogenative coupling of the adjacent methyl groups followed by dehydrogenative aromatization on Cu(111). The molecular structure of the products has been unambiguously revealed by the BRSTM and nc-AFM as shown in Fig. 15D and E.

Notably, nc-AFM image of individual circumcoronene acquired at a moderate tip-sample distance reveals brighter contrast over the corner C–C bonds (yellow arrows), attributed to their higher bond order, which is also consistent with the prediction from its Kekulé structure comprising of the seven Clar's sextets and six double bonds localized at molecular corners. The successful synthesis of [3]coronene will guide the design of elegant precursors for the synthesis of large open-shell coronene homologues.

#### 4.10 Super-heptazethrene

Zethrene with Z-shape geometry was first reported by Clar *et al.* in 1955,<sup>137</sup> (Fig. 1). A unique character of zethrene and expanded zethrenes is the existence of different resonance structures, including closed-shell quinoidal form and open-shell diradical form (Fig. 16A). Although the substituted super-heptazethrene has been synthesized in solution,<sup>138</sup> on-surface synthesis of the unsubstituted super-heptazethrene has been only reported recently.<sup>139</sup>

Fig. 16B presents the precursor design and synthetic strategy of super-heptazethrene. The precursor contains two anthracene

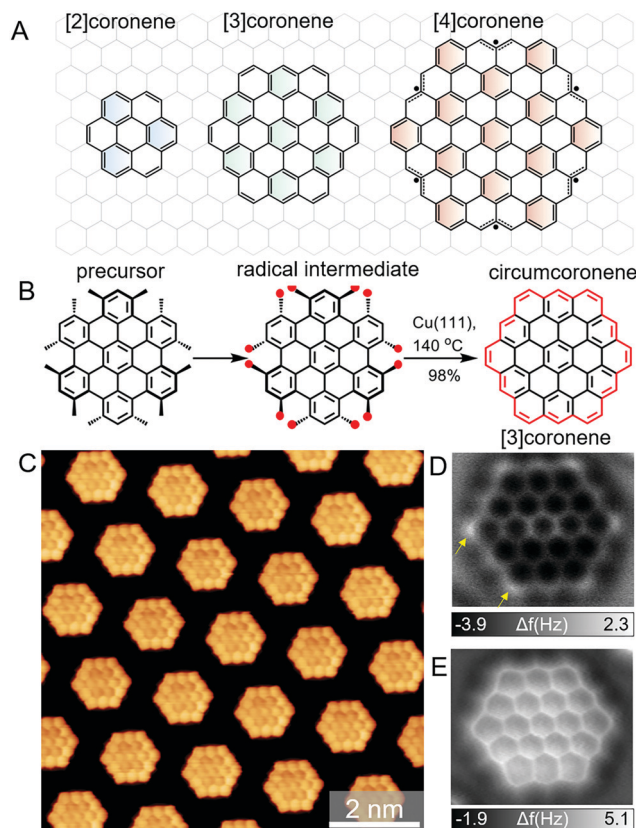
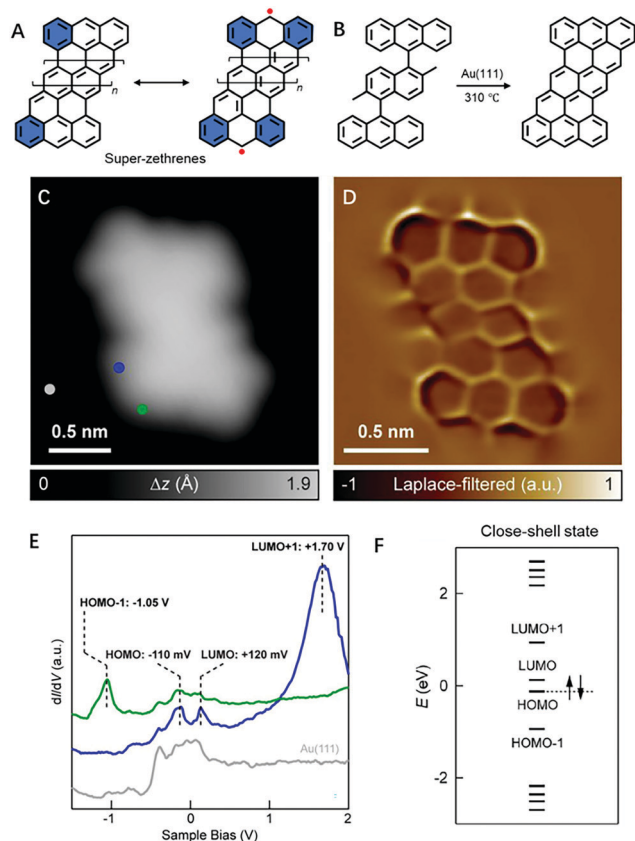


Fig. 15 Synthesis and self-assembly of circumcoronene. (A) A series of hexagonal GNs with six zigzag edges, showing the size dependent magnetic ground state. (B) Schematic illustration of the synthesis of [3]coronene through the cyclodehydrogenation of precursor on Cu(111) via methyl radical-radical coupling towards a high-yield fabrication of the [3]coronene. (B) BRSTM image of as-synthesized circumcoronene-superlattice on Cu(111). (D–E) high-resolution nc-AFM images of individual circumcoronene acquired at a moderate (D) and reduced (E) tip-sample distance. Yellow arrows highlight the brighter contrast over the C=C bonds at the corner, attributed to their higher bond order. Reproduced with permission from ref. 136. Copyright 2020 American Association for the Advancement of Science.

units bridged by a dimethylnaphthalene motif. In addition, the methyl groups are expected to form new zigzag lobes by cyclodehydrogenation. The successful synthesis of super-heptazethrene on Au(111) was confirmed by BRSTM imaging (Laplace-filtered, Fig. 16D).  $dI/dV$  spectrum taken on the super-heptazethrene (the position of  $dI/dV$  spectra was marked in Fig. 16C) reveals apparent features at  $-1.05$  V,  $-110$  mV,  $120$  mV and  $1.7$  V, which can be assigned to HOMO–1, HOMO, LUMO, and LUMO+1 resonances, respectively (Fig. 16E). Although the magnetic ground state of super-zethrene is reported to be open-shell in both solution and solid state, tight-binding (TB) calculation and experimental data reveal a closed-shell ground state on Au(111).

#### 4.11 Porphyrin-based open-shell molecules

In addition to the above-mentioned mechanisms, charge transfer between molecule and substrate can also induce open-shell character in intrinsic closed-shell molecules.<sup>140–142</sup> Recently,



**Fig. 16** On-surface synthesis of super-zethrene. (A) Schematic illustration of the closed-shell Kekulé and open-shell non-Kekulé resonance structures of super-zethrenes. (B) Schematic illustration of the precursor design and on-surface synthetic strategy of super-heptazethrene. (C) High-resolution STM image of super-heptazethrene with a CO-functionalized tip. (D) Corresponding Laplace-filtered BRSTM image of the super-heptazethrene. (E)  $dI/dV$  spectra taken on the super-heptazethrene at the positions marked in (C). (F) Energy spectrum of the super-heptazethrene as predicted by tight-binding mode. Reproduced with permission from ref. 139. Copyright 2019 Royal Society of Chemistry.

Q. Sun *et al.* reported an on-surface synthesis and characterization of two open-shell Zn(II)porphyrins, namely, Zn(II)PorA<sub>2</sub> and Zn(II)PorA<sub>4</sub>, with two and four *meso*, $\beta$ , $\beta$  triply-fused phenalenyl moieties, respectively (Fig. 17D and G).<sup>143</sup>  $dI/dV$  spectrum shows that the characteristic differential conductance steps are symmetrically located in the vicinity of the Fermi level, along with a zero-bias peak (Fig. 17I). The spectrum can be fitted by the dynamical scattering model developed by M. Ternes,<sup>134</sup> which suggests a triplet  $S = 1$  ground state of a molecule. The ferromagnetic (triplet) to antiferromagnetic (singlet) exchange coupling energy (derived from fitting) was estimated to be 19.4 meV. In the case of Zn(II)PorA<sub>4</sub>, both DFT calculation and resonance structure analysis suggest a closed-shell ground state. However, the  $dI/dV$  spectrum (Fig. 17F) shows a pronounced zero-bias resonance which can be ascribed as Kondo resonances due to the presence of an unpaired electron ( $S = \frac{1}{2}$ ). DFT calculations indicate a charge transfer of  $-1.11$  electrons from the molecule to surface as well as a magnetic moment of  $0.69 \mu_B$ , consistent with the  $S = \frac{1}{2}$  ground

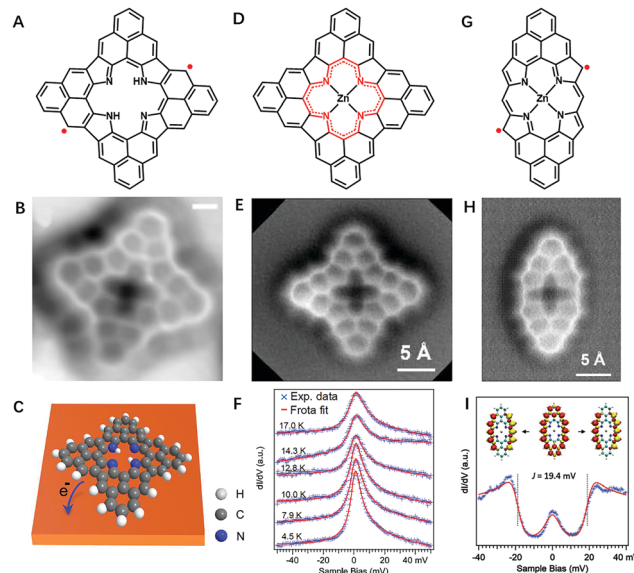


**Fig. 17** Porphyrin-based open-shell molecules. (A, D and G) Chemical structures and the corresponding AFM images (B, E and H) of the on-surface synthesized porphyrin-based open-shell molecules. (C) Illustration of the charge transfer from the neutral molecule to underneath substrate. (F) Temperature dependent  $dI/dV$  spectra of the PorA<sub>4</sub> with the corresponding fitting curve using Frota function ( $V_{\text{mod}} = 0.8$  mV) (I)  $dI/dV$  spectra taken over PorA<sub>2</sub> ( $V_{\text{mod}} = 0.8$  mV). The experimental data (blue) was fitted (red) with dynamical scattering model. Inset shows the spin density plots for the ferromagnetic and antiferromagnetic ground states, where red and yellow colors denote different spin-direction contributions. Reproduced with permission from ref. 143 and 145. Copyright 2020 American Chemical Society.

state. In contrast, the metal-free PorA<sub>4</sub> is predicted to possess an open-shell singlet ( $S = 0$ ) ground state with two unpaired (Fig. 17A) electrons in gas phase by different levels of theoretical calculations.<sup>145</sup> However, charge transfer between PorA<sub>4</sub> and Au(111) substrate also renders it a monoradical ( $S = \frac{1}{2}$ ) character. These examples indicate the charge transfer between organic molecules and substrate act as another approach to induce the open-shell electronic structures of organic molecules on surface.

## 5. Conclusion

Over the last decades, the combination of organic chemistry and on-surface bottom-up synthesis has proved to be a fruitful approach towards the synthesis of numerous ZGNs with appealing electronic and magnetic properties. In general, these unsubstituted ZGNs cannot be obtained *via* the conventional organic synthesis in solution phase but can be precisely fabricated *via* the bottom-up on-surface synthesis thanks to the development of a broad synthetic toolbox in recent years. The advances in scanning probe microscopy allow for submolecular-resolution characterization the structural, electronic, magnetic properties of these ZGNs.

Despite a tremendous progress, several exciting directions deserve more attention. For example, topology engineering of



ZGNs with pentagonal and hexagonal geometries beyond the triangle and rhombus (Fig. 18A) is also intriguing since these molecules are predicted to exhibit open-shell ground state with unique magnetically-coupled edge states.<sup>146</sup> It was also found that larger  $\pi$ -extended systems with fully zigzag edges exhibit larger diradical character than smaller ones owing to the stabilization of the open-shell singlet resonance structures due to the delocalization of  $\pi$ -electrons in larger  $\pi$ -conjugated systems.<sup>147</sup> Moreover, it has been proposed that the decoration of the zigzag edge of nanographene with transition-metal adatoms (*e.g.* ruthenium) can introduce in-plane magnetization in the direction perpendicular to the molecular edge as predicted in the edge-functionalized [8]triangulene molecule (Fig. 18D).<sup>148</sup>

For the ZGNRs, the net spin density on one edge is usually balanced by a spin density of the same amplitude on the other edge, resulting in zero net spin. In this regard, asymmetric

ZGNRs with only one zigzag edge is expected to possess robust ferromagnetic behavior (Fig. 18A).<sup>149</sup> Furthermore, great efforts have been made by theoretical groups to predict novel ZGNs with tunable electronic and magnetic structures by edge functionalization (N, NH<sub>2</sub>, NO<sub>2</sub>, CH<sub>3</sub>) and hetero-atom doping with nitrogen and boron.<sup>150–152</sup> In addition, semiconductor-to-metal transition occurs for wider ZGNRs, which requires the design of novel precursors for the on-surface synthesis.<sup>109</sup> To date, the majority of GNRs synthesized have limited length ( $\sim 50$  nm), presumably due to the inherent short life-time of the radical intermediates. To solve this problem, it is highly desired to take advantage of other non-radical reactions in the toolbox of organic chemistry.<sup>153</sup>

Current progress in the on-synthesis of open-shell GNs mainly involves low-spin GNs with extended zigzag edges or high-spin non-Kekulé GNs. More research attention shall be paid to engineer the magnetism in GNs by intentionally

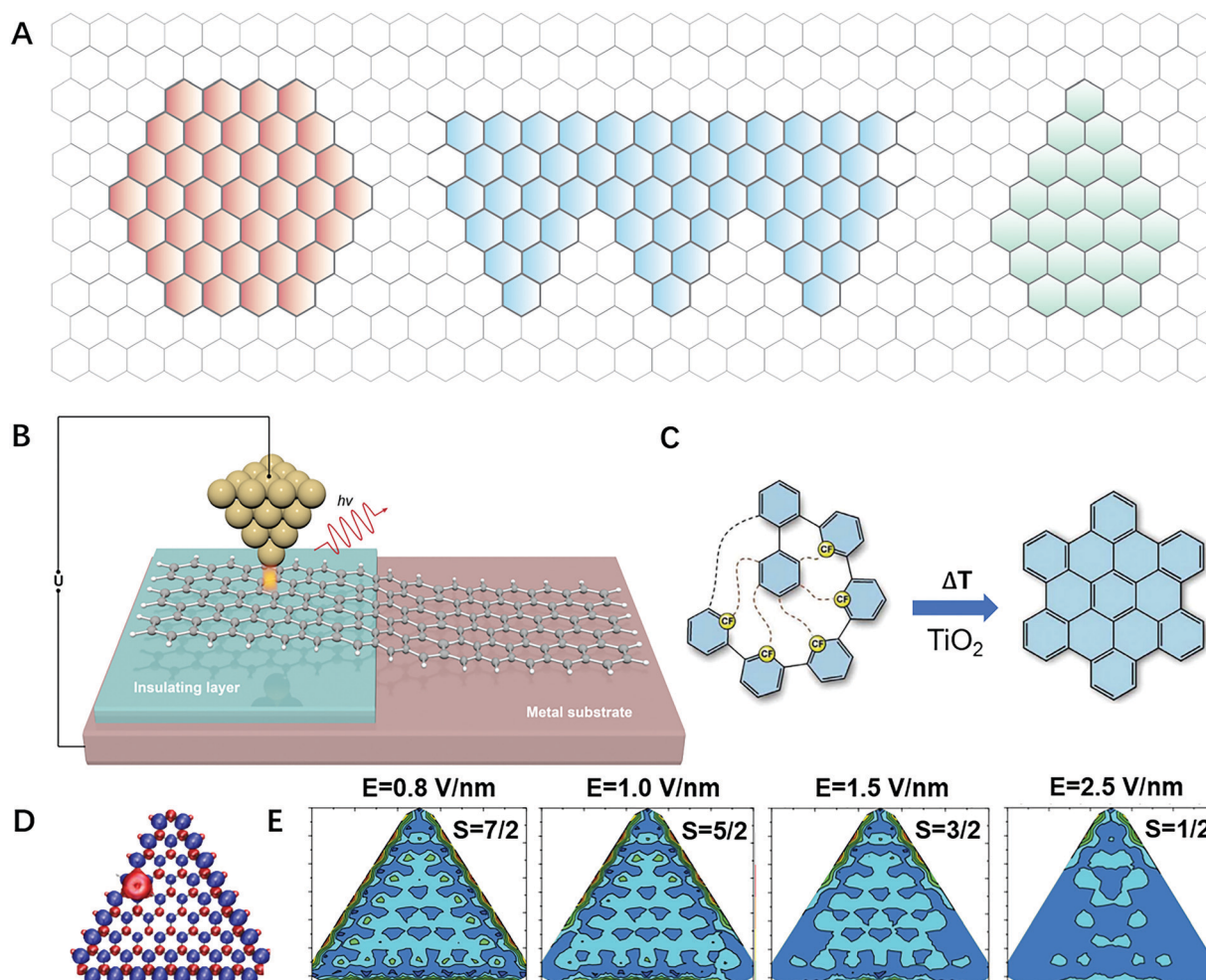


**Fig. 18** (A) The design of new open-shell ZGNs with different geometries including hexagonal and pentagonal ZGMs, and asymmetric ZGNR. (B) Schematic illustration of the transfer of ZGNRs from metal substrate onto insulating substrate for probing their electronic and optical properties. (C) A synthetic strategy of nanographene molecules on insulating surfaces by fluorine-programmed nanozipping. (D) The spin density of ruthenium adatom decorated [8]triangulene the blue and red color indicate different spin configurations. (E) Control the spin density and spin quantum number of [8]triangulene by applying different in-plane electrical fields. Reproduced with permission from ref. 148,162 and 173. Copyright 2013 Beilstein institute for the advancement of chemical sciences (Germany), 2012 American physical society, 2019 American Association for the Advancement of Science.

introducing topological defects, such as non-benzenoid rings. Non-benzenoid rings including five-, seven-, and eight-member rings, are considered as the important structural motifs for tuning the electronic,<sup>154–156</sup> magnetic,<sup>157</sup> and mechanical properties<sup>158–160</sup> of GNs. For example, azulene moiety consisting of a five- and a seven-member ring are often observed in the grain boundaries of graphene or on-surface synthesized closed-shell GNs, which also modify the local electronic properties of the host.<sup>107</sup> In addition, the presence of a five-member ring usually induces a positive Gaussian curvature (such as fullerene), while the presence of a seven- or eight-member ring induces a negative Gaussian curvature, as displayed in Mackay crystals and carbon schwarzite.<sup>161</sup> Theoretical studies also reveal that a schwarzite related structure could carry a net magnetic moment in the ground state. The unpaired electrons are introduced by satirically protected carbon radicals in the aromatic system with a negative Gaussian curvature.<sup>161</sup> Unfortunately, the open-shell GN with non-benzenoid ring synthesized so far is rather limited.<sup>107</sup> It has been reported that they could be synthesized by transforming the sterically stressed precursors into planar GNs on surface *via* strain relief.<sup>144</sup> It is highly desired to design and synthesize more open-shell GNs with non-benzenoid rings to explore their unique electronic and magnetic properties.

In addition, a high level of spin control of these ZGNs by applying in-plane or out-of-plane electric field is critical for unlocking their potential for future spintronic applications.<sup>162</sup> Prior to the application of an in-plane electric field, the spin-up densities are mainly distributed at one particular sublattice of the edge atoms (Fig. 18E). The spin-up and spin-down densities almost compensate each other in the center of the molecule. As the strength of the electric field increases, the total spin decreases and is mainly located in the molecular center. Recent experimental progress has offered new capability to control the charge state of molecules integrated with back-gated graphene devices.<sup>163,164</sup> Therefore, we envision that spin control at the single-molecule level can also be realized through the synthesis of magnetic ZGNs on back-gated devices *via* tip-assisted manipulation.

Additionally, a combination of STM with optical techniques to perform tip-enhanced Raman<sup>165,166</sup> and fluorescence spectroscopy allows for the investigation of the optical properties of GNs at the atomic scale.<sup>167,168</sup> To date, these techniques have been mainly used to study commercially available aromatic molecules and 2D materials such as transition metal dichalcogenides. It will be highly appealing to deploy this technique to explore the quantum emission of ZGNs transferred to the insulating substrates by tip manipulation (Fig. 18B).

The current on-surface synthesis of ZGNs mainly relies on the catalytic role of the metallic substrate to facilitate the chemical reactions. However, for most practical applications, it is required to transfer as-obtained ZGNs onto insulating or semiconducting surfaces. Similar to the transfer protocol established for large-sized graphene, a successful transfer of bottom-up fabricated GNRs from the metal surface onto insulating

substrates for the fabrication of field-effect transistors has been demonstrated.<sup>108,169–172</sup> However, the implementation of this approach to chemically reactive ZGNs in a non-invasive manner remains a challenging task. Inspired by a recent report on the synthesis of armchair-edged graphene nanostructures and polyanthrylene on TiO<sub>2</sub> (Fig. 18C),<sup>173–177</sup> a direct synthesis of atomically-precise ZGNs on an insulating or semiconducting substrate provides an attractive route towards the future device applications. The rapid advancement in both theoretical exploration and experimental realization in this field continuously amazes the material science community, further pushing the boundaries of imagination.

## Conflicts of interest

There are no conflicts to declare.

## Acknowledgements

J. Lu acknowledges the support from MOE grants (MOE2019-T2-2-044, MOE2018-T2-2-094, R-143-000-A75-114) and NRF-CRP grant (NRF-CRP16-2015-02). J. Wu acknowledges the support from MOE grant (MOE2018-T2-2-094). C. Su acknowledges the support from Guangdong Special Support Program, Shenzhen Peacock Plan (KQTD 2016053112042971). M. Telychko acknowledges support from A\*STAR under its AME YIRG Grant (A20E6c0098).

## Notes and references

- 1 A. K. Geim and K. S. Novoselov, in *Nanoscience and technology: a collection of reviews from nature journals*, World Scientific, 2010, pp. 11–19.
- 2 K. S. Novoselov, A. K. Geim, S. V. Morozov, D. Jiang, Y. Zhang, S. V. Dubonos, I. V. Grigorieva and A. A. Firsov, *Science*, 2004, **306**, 666–669.
- 3 K. S. Novoselov, A. K. Geim, S. Morozov, D. Jiang, M. I. Katsnelson, I. Grigorieva, S. Dubonos and A. Firsov, *J. Nat.*, 2005, **438**, 197.
- 4 M. Y. Han, B. Özyilmaz, Y. Zhang and P. Kim, *Phys. Rev. Lett.*, 2007, **98**, 206805.
- 5 J. Lu, P. S. E. Yeo, C. K. Gan, P. Wu and K. P. Loh, *Nat. Nanotechnol.*, 2011, **6**, 247–252.
- 6 J. Lu, A. C. Neto and K. P. Loh, *Nat. Commun.*, 2012, **3**, 1–6.
- 7 J. Fernández-Rossier and J. J. Palacios, *Phys. Rev. Lett.*, 2007, **99**, 177204.
- 8 K. Nakada, M. Fujita, G. Dresselhaus and M. S. Dresselhaus, *Phys. Rev. B: Condens. Matter Mater. Phys.*, 1996, **54**, 17954.
- 9 J. Munárriz, F. Domínguez-Adame and A. Malyshev, *Nanotechnol.*, 2011, **22**, 365201.
- 10 Y.-W. Son, M. L. Cohen and S. G. Louie, *Nature*, 2006, **444**, 347–349.
- 11 H. Şahin, R. T. Senger and S. Ciraci, *J. Appl. Phys.*, 2010, **108**, 074301.

- 12 H. Nagai, M. Nakano, K. Yoneda, H. Fukui, T. Minami, S. Bonness, R. Kishi, H. Takahashi, T. Kubo and K. Kamada, *Chem. Phys. Lett.*, 2009, **477**, 355–359.
- 13 S. Osella, A. Narita, M. G. Schwab, Y. Hernandez, X. Feng, K. Müllen and D. Beljonne, *ACS Nano*, 2012, **6**, 5539–5548.
- 14 O. V. Yazyev, *Rep. Prog. Phys.*, 2010, **73**, 056501.
- 15 P. Ruffieux, S. Wang, B. Yang, C. Sanchez-Sanchez, J. Liu, T. Dienel, L. Talirz, P. Shinde, C. A. Pignedoli, D. Passerone, T. Dumsclaff, X. Feng, K. Müllen and R. Fasel, *Nature*, 2016, **531**, 489–492.
- 16 J. Li, S. Sanz, M. Corso, D. J. Choi, D. Pena, T. Frederiksen and J. I. Pascual, *Nat. Commun.*, 2019, **10**, 200.
- 17 Y. Morita, S. Suzuki, K. Sato and T. Takui, *Nat. Chem.*, 2011, **3**, 197.
- 18 W. L. Wang, O. V. Yazyev, S. Meng and E. Kaxiras, *Phys. Rev. Lett.*, 2009, **102**, 157201.
- 19 E. Clar, *The Aromatic Sextet*, Wiley, New York, 1972.
- 20 M. Solà, *Front. Chem.*, 2013, **1**, 22.
- 21 C. Tao, L. Jiao, O. V. Yazyev, Y.-C. Chen, J. Feng, X. Zhang, R. B. Capaz, J. M. Tour, A. Zettl and S. G. Louie, *Nat. Phys.*, 2011, **7**, 616.
- 22 Q. Ye and C. J. C. O. M. Chi, *Chem. Mater.*, 2014, **26**, 4046–4056.
- 23 A. Narita, X.-Y. Wang, X. Feng and K. Müllen, *Chem. Soc. Rev.*, 2015, **44**, 6616–6643.
- 24 X. Li, X. Wang, L. Zhang, S. Lee and H. Dai, *Science*, 2008, **319**, 1229–1232.
- 25 I. Swart, L. Gross and P. Liljeroth, *Chem. Commun.*, 2011, **47**, 9011–9023.
- 26 N. Pavliček and L. Gross, *Nat. Rev. Chem.*, 2017, **1**, 0005.
- 27 J. Liu and X. Feng, *Angew. Chem., Int. Ed.*, 2020, **59**, 2–18.
- 28 S. Clair and D. G. de Oteyza, *Chem. Rev.*, 2019, **119**, 4717–4776.
- 29 J. Tuček, P. Błoński, J. Ugoletti, A. K. Swain, T. Enoki and R. Zbořil, *Chem. Soc. Rev.*, 2018, **47**, 3899–3990.
- 30 S. Das and J. Wu, *Polycyclic Arenes and Heteroarenes*, John Wiley and Sons, 2015, 1–36.
- 31 T. Jungwirth, X. Marti, P. Wadley and J. Wunderlich, *Nat. Nanotechnol.*, 2016, **11**, 231–241.
- 32 S. Sanvito, *Chem. Soc. Rev.*, 2011, **40**, 3336–3355.
- 33 C. A. Xin-Yi Wang and K. R. Dunbar, *Chem. Soc. Rev.*, 2011, **40**, 3213–3238.
- 34 A. L. F. Lombardi, J. Ma, J. Liu, M. Slota, A. Narita, W. K. Myers, K. Müllen, X. Feng and L. Bogani, *Science*, 2019, **366**, 1107–1110.
- 35 A. K. M. Slota, W. K. Myers, E. Tret'yakov, M. Baumgarten, A. Ardavan, H. Sadeghi, C. J. Lambert, A. Narita, K. Müllen and L. Bogani, *Nature*, 2018, **557**, 691–695.
- 36 O. V. Yazyev, *Nano Lett.*, 2008, **8**, 1011–1015.
- 37 S. M. Wei, L. Wang and E. Kaxiras, *Nano Lett.*, 2008, **8**, 241–245.
- 38 P. P. A. D. Güçlü, O. Voznyy, M. Korkusinski and P. Hawrylak, *Phys. Rev. Lett.*, 2009, **103**, 246805.
- 39 W. Zhang, *Sci. Rep.*, 2014, **4**, 6320.
- 40 A. Saffarzadeh and R. Farghadan, *Appl. Phys. Lett.*, 2011, **98**, 023106.
- 41 T. Ozaki, K. Nishio, H. Weng and H. Kino, *Phys. Rev. B: Condens. Matter Mater. Phys.*, 2010, **81**, 075422.
- 42 V. Karpan, G. Giovannetti, P. Khomyakov, M. Talanana, A. Starikov, M. Zwierzycki, J. Van Den Brink, G. Brocks and P. J. Kelly, *Phys. Rev. Lett.*, 2007, **99**, 176602.
- 43 J. Zeng and K.-Q. Chen, *Phys. Chem. Chem. Phys.*, 2018, **20**, 3997–4004.
- 44 A. Valli, A. Amaricci, V. Brosco and M. Capone, *Nano Lett.*, 2018, **18**, 2158–2164.
- 45 P. P. A. D. Güçlü and P. Hawrylak, *Phys. Rev. B: Condens. Matter Mater. Phys.*, 2011, **84**, 035425.
- 46 S. Zhao, J. Lavie, L. Rondin, L. Orcin-Chaix, C. Diederichs, P. Roussignol, Y. Chassagneux, C. Voisin, K. Müllen and A. Narita, *Nat. Commun.*, 2018, **9**, 1–5.
- 47 G. W. Lingling Li, G. Yang, J. Peng, J. Zhao and J.-J. Zhu, *Nanoscale*, 2013, **5**, 4015–4039.
- 48 R. M.-M. Victor Bonal, F. Gordillo Gámez, M. Morales-Vidal, J. M. Villalvilla, P. G. Boj, J. A. Quintana, Y. Gu, J. Wu, J. Casado and M. A. Díaz-García, *Nat. Commun.*, 2019, **10**, 3327.
- 49 S. T. Qiang Chen, S. Stöttinger, D. Schollmeyer, K. Müllen and T. B. Akimitsu Narita, *J. Am. Chem. Soc.*, 2019, **141**, 16439–16449.
- 50 V. B. Ya Zou, S. Moles Quintero, P. G. Boj, J. M. Villalvilla, J. A. Quintana, G. Li, S. Wu, Q. Jiang, Y. Ni, J. Casado, M. A. Díaz-García and J. Wu, *Angew. Chem., Int. Ed.*, 2020, **59**, 14927–14934.
- 51 L. Grill, M. Dyer, L. Lafferentz, M. Persson, M. V. Peters and S. Hecht, *Nat. Nanotechnol.*, 2007, **2**, 687–691.
- 52 L. Talirz, P. Ruffieux and R. Fasel, *Adv. Mater.*, 2016, **28**, 6222–6231.
- 53 B. Hammer and J. K. Nørskov, *Nature*, 1995, **376**, 238–240.
- 54 Q. Shen, H.-Y. Gao and H. J. N. T. Fuchs, *Nano Today*, 2017, **13**, 77–96.
- 55 M. Treier, C. A. Pignedoli, T. Laino, R. Rieger, K. Müllen, D. Passerone and R. Fasel, *Nat. Chem.*, 2011, **3**, 61.
- 56 S. Mishra, M. Krzeszewski, C. A. Pignedoli, P. Ruffieux, R. Fasel and D. T. Gryko, *Nat. Commun.*, 2018, **9**, 1714.
- 57 J. Gadzuk, *Surf. Sci.*, 1995, **342**, 345–358.
- 58 L. Gross, B. Schuler, N. Pavliček, S. Fatayer, Z. Majzik, N. Moll, D. Peña and G. Meyer, *Angew. Chem., Int. Ed.*, 2018, **57**, 3888–3908.
- 59 J. Krüger, F. García, F. Eisenhut, D. Skidin, J. M. Alonso, E. Guitián, D. Pérez, G. Cuniberti, F. Moresco and D. Peña, *Angew. Chem., Int. Ed.*, 2017, **56**, 11945–11948.
- 60 S. Li, G. Czap, H. Wang, L. Wang, S. Chen, A. Yu, R. Wu and W. Ho, *Phys. Rev. Lett.*, 2019, **122**, 077401.
- 61 E. Kazuma, J. Jung, H. Ueba, M. Trenary and Y. Kim, *J. Am. Chem. Soc.*, 2017, **139**, 3115–3121.
- 62 A. Basagni, L. Colazzo, F. Sedona, M. DiMarino, T. Carofiglio, E. Lubian, D. Forrer, A. Vittadini, M. Casarin and A. Verdini, *Chem. – Eur. J.*, 2014, **20**, 14296–14304.
- 63 X. Y. Zhu and J. White, *J. Chem. Phys.*, 1991, **94**, 1555–1563.
- 64 J. Gadzuk, *J. Chem. Phys.*, 2012, **137**, 678.
- 65 C. Frischkorn and M. Wolf, *Chem. Rev.*, 2006, **106**, 4207–4233.



- 66 C. Lindstrom and X.-Y. Zhu, *Chem. Rev.*, 2006, **106**, 4281–4300.
- 67 F. Eisenhut, T. Kühne, F. García, S. Fernández, E. Guitián, D. Pérez, G. Trinquier, G. Cuniberti, C. Joachim, D. Peña and F. Moresco, *ACS Nano*, 2020, **14**, 1011–1017.
- 68 J. Kruger, N. Pavlicek, J. M. Alonso, D. Perez, E. Guitian, T. Lehmann, G. Cuniberti, A. Gourdon, G. Meyer, L. Gross, F. Moresco and D. Pena, *ACS Nano*, 2016, **10**, 4538–4542.
- 69 J. Krüger, F. Eisenhut, J. M. Alonso, T. Lehmann, E. Guitián, D. Pérez, D. Skidin, F. Gamaleja, D. A. Ryndyk, C. Joachim, D. Peña, F. Moresco and G. Cuniberti, *Chem. Commun.*, 2017, **53**, 1583–1586.
- 70 J. I. Urgel, S. Mishra, H. Hayashi, J. Wilhelm, C. A. Pignedoli, M. Di Giovannantonio, R. Widmer, M. Yamashita, N. Hieda, P. Ruffieux, H. Yamada and R. Fasel, *Nat. Commun.*, 2019, **10**, 861.
- 71 C. F. Laurentiu, E. Dinca, J. M. MacLeod, J. Lipton-Duffin, J. L. Brusso, D. M. Csaba, E. Szakacs, D. F. Perepichka and F. Rosei, *ACS Nano*, 2013, **7**, 1652–1657.
- 72 R. Zuzak, R. Dorel, M. Krawiec, B. Such, M. Kolmer, M. Szymonski, A. M. Echavarren and S. Godlewski, *ACS Nano*, 2017, **11**, 9321–9329.
- 73 R. Zuzak, R. Dorel, M. Kolmer, M. Szymonski, S. Godlewski and A. M. Echavarren, *Angew. Chem., Int. Ed.*, 2018, **57**, 10500–10505.
- 74 N. Pavlicek, A. Mistry, Z. Majzik, N. Moll, G. Meyer, D. J. Fox and L. Gross, *Nat. Nanotechnol.*, 2017, **12**, 308–311.
- 75 B. Schuler, W. Liu, A. Tkatchenko, N. Moll, G. Meyer, A. Mistry, D. Fox and L. Gross, *Phys. Rev. Lett.*, 2013, **111**, 106103.
- 76 M. Bendikov, H. M. Duong, K. Starkey, K. Houk, E. A. Carter and F. Wudl, *J. Am. Chem. Soc.*, 2004, **126**, 7416–7417.
- 77 K. Houk, P. S. Lee and M. J. T. Nendel, *J. Org. Chem.*, 2001, **66**, 5517–5521.
- 78 M. Dos Santos, *J. Phys. Rev. B.*, 2006, **74**, 045426.
- 79 Y. Yang, E. R. Davidson and W. Yang, *Proc. Natl. Acad. Sci. U. S. A.*, 2016, **113**, 5098–5107.
- 80 F. Plasser, H. Pašalić, M. H. Gerzabek, F. Libisch, R. Reiter, J. Burgdörfer, T. Müller, R. Shepard and H. Lischka, *Angew. Chem., Int. Ed.*, 2013, **52**, 2581–2584.
- 81 J. Hachmann, J. J. Dorando, M. Avilés and G. K.-L. J. T. Chan, *J. Chem. Phys.*, 2007, **127**, 134309.
- 82 D. Jiang and S. J. T. Dai, *J. Phys. Chem.*, 2008, **112**, 332–335.
- 83 M. Bendikov, F. Wudl and D. F. Perepichka, *Chem. Rev.*, 2004, **104**, 4891–4946.
- 84 J. E. Anthony, *Chem. Rev.*, 2006, **106**, 5028–5048.
- 85 R. A. Pascal, *Chem. Rev.*, 2006, **106**, 4809–4819.
- 86 J. E. Anthony, *Angew. Chem., Int. Ed.*, 2008, **47**, 452–483.
- 87 Z. Sun, Q. Ye, C. Chi and J. Wu, *J. Chem. Soc. Rev.*, 2012, **41**, 7857–7889.
- 88 M. Watanabe, K.-Y. Chen, Y. J. Chang and T. Chow, *Acc. Chem. Res.*, 2013, **46**, 1606–1615.
- 89 M. M. Payne, S. R. Parkin and J. E. Anthony, *J. Am. Chem. Soc.*, 2005, **127**, 8028–8029.
- 90 D. Chun, Y. Cheng and F. Wudl, *Angew. Chem., Int. Ed.*, 2008, **120**, 8508–8513.
- 91 H. Qu and C. Chi, *Org. Lett.*, 2010, **12**, 3360–3363.
- 92 J. E. Anthony, *Angew. Chem., Int. Ed.*, 2008, **47**, 452–483.
- 93 R. Zuzak, R. Dorel, M. Krawiec, B. Such, M. Kolmer, M. Szymonski, A. M. Echavarren and S. Godlewski, *ACS Nano*, 2017, **11**, 9321–9329.
- 94 B. Hajgato, M. S. Deleuze, D. J. Tozer and F. De Proft, *J. Chem. Phys.*, 2008, **129**, 084308.
- 95 J. I. Urgel, H. Hayashi, M. Di Giovannantonio, C. A. Pignedoli, S. Mishra, O. Deniz, M. Yamashita, T. Dienel, P. Ruffieux, H. Yamada and R. Fasel, *J. Am. Chem. Soc.*, 2017, **139**, 11658–11661.
- 96 C. Sanchez-Sanchez, A. Nicolai, F. Rossel, J. Cai, J. Liu, X. Feng, K. Müllen, P. Ruffieux, R. Fasel and V. Meunier, *J. Am. Chem. Soc.*, 2017, **139**, 17617–17623.
- 97 E. Clar, *Aromatic Sextet*, New York, Wiley, 1972.
- 98 N. Friedrich, P. Brandimarte, J. Li, S. Saito, S. Yamaguchi, I. Pozo, D. Peña, T. Frederiksen, A. Garcia-Lekue, D. Sánchez-Portal and J. I. Pascual, *Phys. Rev. Lett.*, 2020, **125**, 146801.
- 99 Z. Sun, Z. Zeng and J. Wu, *Acc. Chem. Res.*, 2014, **47**, 2582–2591.
- 100 Y. Ni, T. Y. Gopalakrishna, H. Phan, T. S. Herng, S. Wu, Y. Han, J. Ding and J. Wu, *Angew. Chem., Int. Ed.*, 2018, **130**, 9845–9849.
- 101 X. Y. Wang, T. Dienel, M. Di Giovannantonio, G. B. Barin, N. Kharche, O. Deniz, J. I. Urgel, R. Widmer, S. Stolz, L. H. De Lima, M. Muntwiler, M. Tommasini, V. Meunier, P. Ruffieux, X. Feng, R. Fasel, K. Müllen and A. Narita, *J. Am. Chem. Soc.*, 2017, **139**, 4671–4674.
- 102 S. Mishra, T. G. Lohr, C. A. Pignedoli, J. Liu, R. Berger, J. I. Urgel, K. Müllen, X. Feng, P. Ruffieux and R. Fasel, *ACS Nano*, 2018, **12**, 11917–11927.
- 103 C. Rogers, C. Chen, Z. Pedramrazi, A. A. Omrani, H. Z. Tsai, H. S. Jung, S. Lin, M. F. Crommie and F. R. Fischer, *Angew. Chem., Int. Ed.*, 2015, **54**, 15143–15146.
- 104 J. Cai, P. Ruffieux, R. Jaafar, M. Bieri, T. Braun, S. Blankenburg, M. Muoth, A. P. Seitsonen, M. Saleh, X. J. N. Feng, K. Müllen and R. Fasel, *Nature*, 2010, **466**, 470–473.
- 105 S. Kawai, S. Saito, S. Osumi, S. Yamaguchi, A. S. Foster, P. Spijker and E. J. N. C. Meyer, *Nat. Commun.*, 2015, **6**, 1–6.
- 106 Y.-C. Chen, T. Cao, C. Chen, Z. Pedramrazi, D. Haberer, D. G. De Oteyza, F. R. Fischer, S. G. Louie and M. F. Crommie, *Nat. Nanotechnol.*, 2015, **10**, 156.
- 107 J. Liu, B.-W. Li, Y.-Z. Tan, A. Giannakopoulos, C. Sanchez-Sanchez, D. Beljonne, P. Ruffieux, R. Fasel, X. Feng and K. Müllen, *J. Am. Chem. Soc.*, 2015, **137**, 6097–6103.
- 108 H. Sakaguchi, S. Song, T. Kojima and T. Nakae, *Nat. Chem.*, 2017, **9**, 57.
- 109 G. Z. Magda, X. Jin, I. Hagymasi, P. Vancso, Z. Osvath, P. Nemes-Incze, C. Hwang, L. P. Biro and L. Tapasztó, *Nature*, 2014, **514**, 608–611.
- 110 S. Kawai, S. Saito, S. Osumi, S. Yamaguchi, A. S. Foster, P. Spijker and E. Meyer, *Nat. Commun.*, 2015, **6**, 8098.
- 111 H. Huang, D. Wei, J. Sun, S. L. Wong, Y. P. Feng, A. C. Neto and A. T. S. Wee, *Sci. Rep.*, 2012, **2**, 983.
- 112 A. Basagni, F. Sedona, C. A. Pignedoli, M. Cattelan, L. Nicolas, M. Casarin and M. Sambi, *J. Am. Chem. Soc.*, 2015, **137**, 1802–1808.

- 113 S. Mishra, D. Beyer, K. Eimre, S. Kezilebieke, R. Berger, O. Gröning, C. A. Pignedoli, K. Müllen, P. Liljeroth, P. Ruffieux, X. Feng and R. Fasel, *Nat. Nanotechnol.*, 2020, **15**, 22–28.
- 114 D. Beyer, S. Wang, C. A. Pignedoli, J. Melidonie, B. Yuan, C. Li, J. Wilhelm, P. Ruffieux, R. Berger, K. Müllen, R. Fasel and X. Feng, *J. Am. Chem. Soc.*, 2019, **141**, 2843–2846.
- 115 A. E. Miroshnichenko, S. Flach and Y. S. Kivshar, *Rev. Mod. Phys.*, 2010, **82**, 2257.
- 116 Y. Wang, X. Zheng and J. Yang, *Phys. Rev. B*, 2016, **93**, 125114.
- 117 L. Gao, W. Ji, Y. Hu, Z. Cheng, Z. Deng, Q. Liu, N. Jiang, X. Lin, W. Guo, S. X. Du, W. A. Hofer, X. C. Xie and H.-J. Gao, *Phys. Rev. Lett.*, 2007, **99**, 106402.
- 118 X. Li, L. Zhu, B. Li, J. Li, P. Gao, L. Yang, A. Zhao, Y. Luo, J. Hou and X. Zheng, *Nat. Commun.*, 2020, **11**, 1–8.
- 119 S. Wang, L. Talirz, C. A. Pignedoli, X. Feng, K. Müllen, R. Fasel and P. Ruffieux, *Nat. Commun.*, 2016, **7**, 11507.
- 120 L. Talirz, H. Sode, J. Cai, P. Ruffieux, S. Blankenburg, R. Jafaar, R. Berger, X. Feng, K. Müllen, D. Passerone, R. Fasel and C. A. Pignedoli, *J. Am. Chem. Soc.*, 2013, **135**, 2060–2063.
- 121 J. Lawrence, P. Brandimarte, A. Berdonces-Layunta, M. S. Mohammed, A. Grewal, C. C. Leon, D. Sanchez-Portal and D. G. de Oteyza, *ACS Nano*, 2020, **14**, 4499–4508.
- 122 M. Huzak, M. Deleuze and B. Hajgató, *J. Chem. Phys.*, 2011, **135**, 104704.
- 123 A. D. Zdetsis, *J. Phys. Chem. C*, 2020, **124**, 7578–7584.
- 124 J. Repp, G. Meyer, S. M. Stojković, A. Gourdon and C. Joachim, *Phys. Rev. Lett.*, 2005, **94**, 026803.
- 125 J. Su, M. Telychko, S. Song and J. Lu, *Angew. Chem., Int. Ed.*, 2020, **132**, 7730–7740.
- 126 J. Su, W. Fan, P. Mutombo, X. Peng, S. Song, M. Telychko, P. Jelinek, J. Wu and J. Lu, *Nano Lett.*, 2020, **21**, 861–867.
- 127 H.-X. Yang, M. Chshiev, D. W. Boukhvalov, X. Waintal and S. Roche, *Phys. Rev. B: Condens. Matter Mater. Phys.*, 2011, **84**, 214404.
- 128 T. G. Pedersen, C. Flindt, J. Pedersen, N. A. Mortensen, A.-P. Jauho and K. Pedersen, *Phys. Rev. Lett.*, 2008, **100**, 136804.
- 129 S. Mishra, D. Beyer, K. Eimre, R. Ortiz, J. Fernández-Rossier, R. Berger, O. Gröning, C. Pignedoli, R. Fasel and X. Feng, *Angew. Chem., Int. Ed.*, 2020, **59**, 12041.
- 130 J. Li, S. Sanz, J. Castro-Esteban, M. Vilas-Varela, N. Friedrich, T. Frederiksen, D. Peña and J. I. Pascual, *Phys. Rev. Lett.*, 2019, **124**, 177201.
- 131 S. Mishra, D. Beyer, R. Berger, J. Liu, O. Groening, J. I. Urgel, K. Müllen, P. Ruffieux, X. Feng and R. Fasel, *J. Am. Chem. Soc.*, 2020, **142**, 1147–1152.
- 132 E. Clar and C. Mackay, *Tetrahedron*, 1972, **28**, 6041–6047.
- 133 C. F. Hirjibehedin, C. P. Lutz and A. J. Heinrich, *Science*, 2006, **312**, 1021–1024.
- 134 M. J. Ternes, *New J. Phys.*, 2015, **17**, 063016.
- 135 S. Mishra, X. Yao, Q. Chen, K. Eimre, O. Groening, R. Ortiz, M. Di Giovannantonio, J. C. Sancho-Garcia, J. Fernandez-Rossier, C. A. Pignedoli, K. Müllen, P. Ruffieux, A. Narita and R. Fasel, 2020, arXiv:2003.03577.
- 136 M. Telychko, G. Li, P. Mutombo, D. Soler-Polo, X. Peng, J. Su, S. Song, M. J. Koh, M. Edmonds, P. Jelinek and J. Lu, *Sci. Adv.*, 2021, **7**, eabf0269.
- 137 E. Clar, K. F. Lang and H. Schulz-Kiesow, *Chem. Ber.*, 1955, **88**, 1520–1527.
- 138 W. Zeng, Z. Sun, T. S. Herng, T. P. Gonçalves, T. Y. Gopalakrishna, K. W. Huang, J. Ding and J. Wu, *Angew. Chem., Int. Ed.*, 2016, **55**, 8615–8619.
- 139 S. Mishra, J. Melidonie, K. Eimre, S. Obermann, O. Gröning, C. A. Pignedoli, P. Ruffieux, X. Feng and R. Fasel, *Chem. Commun.*, 2020, **56**, 7467–7470.
- 140 A. Kumar, K. Banerjee, M. Dvorak, F. Schulz, A. Harju, P. Rinke and P. Liljeroth, *ACS Nano*, 2017, **11**, 4960–4968.
- 141 M. Garnica, D. Stradi, S. Barja, F. Calleja, C. Díaz, M. Alcamí, N. Martín, A. L. V. De Parga, F. Martín and R. Miranda, *Nat. Phys.*, 2013, **9**, 368–374.
- 142 I. Fernández-Torrente, D. Kreikemeyer-Lorenzo, A. Stróżecka, K. J. Franke and J. I. Pascual, *Phys. Rev. Lett.*, 2012, **108**, 036801.
- 143 Q. Sun, L. M. Mateo, R. Robles, P. Ruffieux, N. Lorente, G. Bottari, T. Torres and R. Fasel, *J. Am. Chem. Soc.*, 2020, **142**, 18109–18117.
- 144 A. Shiotari, T. Nakae, K. Iwata, S. Mori, T. Okujima, H. Uno, H. Sakaguchi and Y. Sugimoto, *Nat. Commun.*, 2017, **8**, 16089.
- 145 Y. Zhao, K. Jiang, C. Li, Y. Liu, C. Xu, W. Zheng, D. Guan, Y. Li, H. Zheng, C. Liu, W. Luo, J. Jia, X. Zhuang and S. Wang, *J. Am. Chem. Soc.*, 2020, **142**, 18532–18540.
- 146 M. Nakano, *Top. Curr. Chem.*, 2017, **375**, 47.
- 147 Y. Gu, X. Wu, T. Y. Gopalakrishna, H. Phan and J. J. A. C. Wu, *Angew. Chem., Int. Ed.*, 2018, **130**, 6651–6655.
- 148 I. Beljakov, V. Meded, F. Symalla, K. Fink, S. Shallcross and W. Wenzel, *Beilstein J. Nanotechnol.*, 2013, **4**, 441–445.
- 149 D. J. Adams, O. Gröning, C. A. Pignedoli, P. Ruffieux, R. Fasel and D. Passerone, *Phys. Rev. B: Condens. Matter Mater. Phys.*, 2012, **85**, 245405.
- 150 S. Dutta, A. K. Manna and S. K. Pati, *Phys. Rev. Lett.*, 2009, **102**, 096601.
- 151 E.-j. Kan, Z. Li, J. Yang and J. Hou, *J. Am. Chem. Soc.*, 2008, **130**, 4224–4225.
- 152 Y. Wang, Y. Ding, S. Shi and W. Tang, *Appl. Phys. Lett.*, 2011, **98**, 163104.
- 153 A. Gourdon, *Angew. Chem., Int. Ed.*, 2008, **47**, 6950–6953.
- 154 J. Červenka and C. Flipse, *Phys. Rev. B: Condens. Matter Mater. Phys.*, 2009, **79**, 195429.
- 155 N. Peres, F. Guinea and A. C. Neto, *Phys. Rev. B: Condens. Matter Mater. Phys.*, 2006, **73**, 125411.
- 156 A. Mesaros, S. Papanikolaou, C. Flipse, D. Sadri and J. Zaanen, *Phys. Rev. B: Condens. Matter Mater. Phys.*, 2010, **82**, 205119.
- 157 J. Červenka, M. Katsnelson and C. Flipse, *Nat. Phys.*, 2009, **5**, 840–844.
- 158 Y. Liu and B. I. Yakobson, *Nano Lett.*, 2010, **10**, 2178–2183.
- 159 R. Grantab, V. B. Shenoy and R. S. Ruoff, *Science*, 2010, **330**, 946–948.
- 160 O. V. Yazyev and S. G. Louie, *Phys. Rev. B: Condens. Matter Mater. Phys.*, 2010, **81**, 195420.

- 161 N. Park, M. Yoon, S. Berber, J. Ihm, E. Osawa and D. Tománek, *Phys. Rev. Lett.*, 2003, **91**, 237204.
- 162 W.-L. Ma and S.-S. Li, *Phys. Rev. B: Condens. Matter Mater. Phys.*, 2012, **86**, 045449.
- 163 S. Wickenburg, J. Lu, J. Lischner, H.-Z. Tsai, A. A. Omrani, A. Riss, C. Karrasch, A. Bradley, H. S. Jung, R. Khajeh, D. Wong, K. Watanabe, T. Taniguchi, A. Zettl, A. H. Castro Neto, S. G. Louie and M. F. Crommie, *Nat. Commun.*, 2016, **7**, 13553.
- 164 J. Lu, H.-Z. Tsai, A. N. Tatan, S. Wickenburg, A. A. Omrani, D. Wong, A. Riss, E. Piatti, K. Watanabe and T. Taniguchi, *Nat. Commun.*, 2019, **10**, 477.
- 165 T. Schmid, L. Opilik, C. Blum and R. Zenobi, *Angew. Chem., Int. Ed.*, 2013, **52**, 5940–5954.
- 166 R. Zhang, Y. Zhang, Z. Dong, S. Jiang, C. Zhang, L. Chen, L. Zhang, Y. Liao, J. Aizpurua and Y. Luo, *Nature*, 2013, **498**, 82–86.
- 167 Y. Zhang, Y. Luo, Y. Zhang, Y.-J. Yu, Y.-M. Kuang, L. Zhang, Q.-S. Meng, Y. Luo, J.-L. Yang and Z.-C. Dong, *Nature*, 2016, **531**, 623–627.
- 168 K. Kimura, K. Miwa, H. Imada, M. Imai-Imada, S. Kawahara, J. Takeya, M. Kawai, M. Galperin and Y. Kim, *Nature*, 2019, **570**, 210–213.
- 169 J. Cai, C. A. Pignedoli, L. Talirz, P. Ruffieux, H. Söde, L. Liang, V. Meunier, R. Berger, R. Li and X. J. Feng, *Nat. Nanotechnol.*, 2014, **9**, 896.
- 170 J. Cai, P. Ruffieux, R. Jaafar, M. Bieri, T. Braun, S. Blankenburg, M. Muoth, A. P. Seitsonen, M. Saleh and X. Feng, *Nature*, 2010, **466**, 470.
- 171 P. B. Bennett, Z. Pedramrazi, A. Madani, Y.-C. Chen, D. G. de Oteyza, C. Chen, F. R. Fischer, M. F. Crommie and J. Bokor, *Appl. Phys. Lett.*, 2013, **103**, 253114.
- 172 S. Zhao, G. Borin Barin, L. Rondin, C. Raynaud, A. Fairbrother, T. Dumsloff, S. Campidelli, K. Müllen, A. Narita and C. Voisin, *Phys. Status Solidi B*, 2017, **254**, 1700223.
- 173 M. Kolmer, R. Zuzak, A.-K. Steiner, L. Zajac, M. Engelund, S. Godlewski, M. Szymonski and K. Amsharov, *Science*, 2019, **363**, 57–60.
- 174 M. Kolmer, A. A. Ahmad Zebari, J. S. Prauzner-Bechcicki, W. Piskorz, F. Zasada, S. Godlewski, B. Such, Z. Sojka and M. Szymonski, *Angew. Chem., Int. Ed.*, 2013, **125**, 10490–10493.
- 175 M. Kolmer, R. Zuzak, A. A. A. Zebari, S. Godlewski, J. S. Prauzner-Bechcicki, W. Piskorz, F. Zasada, Z. Sojka, D. Bléger and S. Hecht, *Chem. Commun.*, 2015, **51**, 11276–11279.
- 176 G. Vasseur, M. Abadia, L. A. Miccio, J. Brede, A. Garcia-Lekue, D. G. de Oteyza, C. Rogero, J. Lobo-Checa and J. E. Ortega, *J. Am. Chem. Soc.*, 2016, **138**, 5685–5692.
- 177 M. Kolmer, A.-K. Steiner, I. Izydorczyk, W. Ko, M. Engelund, M. Szymonski, A.-P. Li and K. Amsharov, *Science*, 2020, **369**, 571–575.